Modular Stator Flux and Torque Control of Multi-Three-Phase Induction Motor Drives

Modular Stator Flux and Torque Control of Multi-Three-Phase Induction Motor Drives

Sandro Rubino, *Member*, *IEEE,* Radu Bojoi, *Fellow*, *IEEE,* Fabio Mandrile, *Student Member*, *IEEE,*
and Eric Armando, *Senior Member*, *IEEE*
Dipartimento Energia "G. Ferraris"
Politecnico di Torino
Torino, 10129, Italy

***Abstract*—The recent advancements of power electronics are encouraging the development of the multiphase drives in both transport electrification and energy production applications. Among the multiphase solutions, the "multi-three-phase" drives are gaining impressive attention from the industry since they can be configured as multiple three-phase units operating in parallel. In this way, the three-phase technologies can be used, leading to a significant reduction in the costs and design time. Although the multi-three-phase drives possess natural modularity in terms of both machine winding and power converter, few control solutions able to implement a modular regulation of the torque are available in the literature. Therefore, this paper proposes a control scheme implementing an independent regulation of the stator flux amplitude and torque contribution belonging to each winding set of a multi-three-phase induction machine. The proposed control solution can manage the voltage and current constraints introduced by each inverter unit. Besides, torque-sharing strategies among the three-phase sets of the machine can be implemented. Experimental results are provided for a modular power converter feeding a twelve-phase induction machine with a quadruple-three-phase configuration, thus demonstrating the effectiveness of the proposed solution.**

Keywords— direct flux vector control, induction motor drives, modular torque control, multiphase electrical machines.

NOMENCLATURE

p	Pole pairs number.
n	Number of three-phase sets.
k, z	Index of a generic set. (k = 1,2,…,n) ; (z = 1,2,…,n).
$(abc)_k$	k-set phase coordinates.
$(\alpha\beta)$	Stationary coordinates.
(dq_e)	Rotor electric coordinates.
(dq_{sk})	k-set flux coordinates.
(xy)	Generic coordinates (any of the above).
a_{sk}	First phase of set k.
ϑ_{sk}	Magnetic position of the k-set first phase to the α-axis.
$[T_{C,k}]$	General Clarke transformation.
$\bar{v}_{sk,xy} = [v_{sk,x}\ v_{sk,y}]^t$	k-set voltage vector defined in (xy) coordinates.
$\bar{\imath}_{sk,xy} = [i_{sk,x}\ i_{sk,y}]^t$	k-set current vector defined in (xy) coordinates.
$\bar{\lambda}_{sk,xy} = [\lambda_{sk,x}\ \lambda_{sk,y}]^t$	k-set flux linkage vector defined in (xy) coordinates.
R_{sk}	k-set resistance.
L_{lsk}	k-set leakage inductance.
ω_{xy}	Synchronous speed of the (xy) frame.
L_m	Magnetizing inductance.
$j = \begin{bmatrix} 0 & -1 \\ 1 & 0 \end{bmatrix}$	Matrix form of complex operator.
$\bar{\imath}_{r,xy} = [i_{r,x}\ i_{r,y}]^t$	Rotor current vector defined in (xy) coordinates.
$\bar{\lambda}_{r,xy} = [\lambda_{r,x}\ \lambda_{r,y}]^t$	Rotor flux linkage vector defined in (xy) coordinates.
R_r	Rotor resistance.
L_{lr}	Rotor leakage inductance.
$k_r = L_m / (L_m + L_{lr})$	Rotor coupling factor.
$k_{sk} = L_m / (L_m + L_{lsk})$	k-set coupling factor.
$\tau_r = (L_m + L_{lr}) / R_r$	Rotor time-constant.
ϑ_m	Mechanical position of the rotor.
$\vartheta_e = p \cdot \vartheta_m$	Electrical position of the rotor to the α-axis.
ω_m	Mechanical speed of the rotor.
$\omega_e = p \cdot \omega_m$	Electrical speed of the rotor.
T_k	k-set torque contribution.
$T = \sum_{k=1}^{n} T_k$	Machine torque.
P_m	Mechanical power.
$x_{f,k}$, $x_{f,z}$	Status of the generic unit k, z (0-faulty/1-active).
w_z , c_k	Coupling coefficients.
L_k	k-set equivalent inductance.
R_k	k-set equivalent resistance.
M_k	k-set equivalent mutual reactance in (xy) coordinates.
P_z	Mutual resistance between the set k and set z ($k \neq z$).
Q_z	Mutual reactance between the set k and set z ($k \neq z$).
$F_{sk,x}$, $F_{sk,y}$	Voltage forcings terms in (xy) coordinates of the set k.
$v_{dc,k}$	k-unit dc-link voltage.
$I_{max,k}$	Amplitude limit of the k-set phase-currents.
$[i_{sk,abc}] = [i_{sk\text{-}a}\ i_{sk\text{-}b}\ i_{sk\text{-}c}]^t$	k-set phase-currents.
τ	Superscript – generic sampling time instant.
*	Superscript – reference variable.
$\hat{}$	Superscript – observed variable.
$\tilde{}$	Superscript – estimated variable.
$[d^*_{k,abc}]=[d^*_{k,a}\ d^*_{k,b}\ d^*_{k,c}]^t$	k-unit duty-cycles.
λ_{sk}	Amplitude of the k-set flux vector.
$\vartheta_{\lambda\text{-}sk}$	Position of the k-set flux vector to the α-axis.
δ_{sk}	k-set load-angle.
$\delta_{max,k}$	Limit of the k-set load-angle.
$\bar{F}_{sk}$	Reference voltage forcings terms of the set k in (dq_{sk}) coordinates.
$\omega_{c,k}$	Gain of the k-unit flux observer.

ω_{sk}	Synchronous speed of the (dq_{sk}) frame.
$\vartheta_{\lambda\text{-}r}$	Position of the rotor flux vector to the α-axis.
$v_{sk\text{-}max}$	Amplitude limit of the k-unit phase-voltages.
$\lambda_{sk\text{-}max}$	Amplitude limit of the k-set flux vector.
$i_{sk,q_{sk}-max\ i}$	Saturation limit of the k-set torque current $i_{sk,q_{sk}}$, due to $I_{max,k}$.
$\bar{\lambda}_{mk,xy} = [\lambda_{mk,x}\ \lambda_{mk,y}]^t$	k-set magnetizing flux vector defined in (xy) coordinates.
λ_{mk}	Amplitude of the k-set magnetizing flux vector $\bar{\lambda}_{mk}$.
$\vartheta_{\lambda\text{-}mk}$	Position of the k-set magnetizing flux vector $\bar{\lambda}_{mk}$ to the α-axis.
$L_{\sigma k}$	k-set overall leakage inductance.
$i_{sk,q_{sk}-lim\ \delta}\big\vert_{min}$	Low saturation limit of the k-set torque current $i_{sk,q_{sk}}$, due to $\delta_{max,k}$.
$i_{sk,q_{sk}-lim\ \delta}\big\vert^{max}$	High saturation limit of the k-set torque current $i_{sk,q_{sk}}$, due to $\delta_{max,k}$.
$v_{sk,q_{sk}-max}$	Operative range of the k-unit q_{sk}-axis voltage component.
$C^*_{sk,q_{sk}}$	k-unit combination of the reference voltages of all sets referred to the q_{sk}-axis.
$s_{(k,k)}$, $s_{(k,z)}$	Decoupling coefficients.
S_c, $S_{k\text{-}k}$, $S_{k\text{-}z}$	Variables of the decoupling algorithm.
$[v^*_{sk,abc}]=[v^*_{sk,a}\ v^*_{sk,b}\ v^*_{sk,c}]^t$	k-unit reference phase-voltages.

I. Introduction

In recent years, multiphase drives have become a competitive solution for both transport electrifications and energy production from renewables [1], [2]. Compared to the three-phase counterparts, multiphase machines allow at reducing the current per phase without increasing the phase-voltage, making possible the use of fast electronic devices also in high power applications. Besides, the reliability of the system increases, as fault-tolerant strategies can be implemented [3], [4]. Such advantages, together with a significant cost reduction of the power electronics devices, have made multiphase drives promising solutions for the future electrification processes.

Based on the current technological trend [2], [5], [6], significant interest has been shown on multiphase machines having phases number multiple of three (e.g., 6, 9, 12,...). In this case, the machine stator can be configured as multiple three-phase winding sets with isolated neutral points, obtaining a so-called "multi-three-phase" machine. In this way, each three-phase set can be fed by an independent voltage source inverter (VSI), defining a multi-three-phase drive topology that is schematically shown in Fig. 1. The advantages of such a system are evident since the consolidated three-phase technologies can be used, reducing cost and design time. Another advantage of the multi-three-phase drives consists of extending the three-phase modularity also in terms of fault-tolerance. Indeed, if an open-phase fault event occurs on the machine side or the inverter side, the faulted three-phase unit (winding set plus VSI) is disconnected from its dc power supply, allowing a straightforward post-fault drive reconfiguration [2], [5], [7].

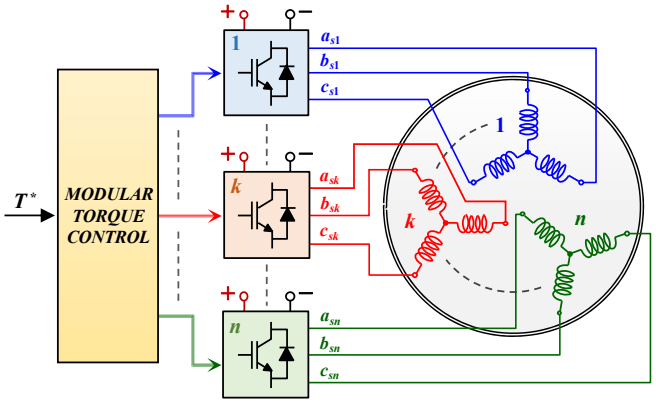

Fig. 1. Multi-three-phase drive topology.

The multi-three-phase machines are usually designed to operate with a balanced operation of the units [8]–[11]. However, the literature reports significant examples in which power-sharing strategies among the sets can be performed [12]–[14]. Although this operation leads to the reduction of the overall machine efficiency [15], it results quite useful in the "series/parallel" configurations [15], [16]. As an example, the solutions presented in [16], [17] employ multi-three-phase generators with the series-connection of the units' dc-link, thus forming a high voltage dc (HVDC) transmission system. Such structures may have a great interest in the offshore wind farms where HVDC systems are usually employed [18].

Nevertheless, the literature reports a few drive control schemes able to implement direct and independent control of each three-phase unit. In detail, most of the presented solutions perform power-sharing indirect strategies among the sets through the current-sharing, i.e., regulation of the units' currents using field-oriented control (FOC) schemes [12]–[14]. Besides, since the multi-three-phase machines represent a specific multiphase configuration, the vector space decomposition (VSD) approach has often been applied [15], [19], [20].

The VSD-based control schemes perform the energy conversion in an average (d,q) subspace, having the meaning of the time-fundamental model of the machine. The power- or current- sharing strategies among the sets are performed through the active control of the other subspaces [12], [14], [15], representing time-harmonic models of the machine. The advantages of such an approach are evident since the drive control can be performed as for the conventional three-phase machines, thus avoiding any coupling phenomena among the sets [21].

The literature also reports VSD-based direct torque control (DTC) algorithms using switching tables [22], [23]. However, based on the authors' best knowledge, the literature does not report DTC solutions performing the post-fault operation of the machine after an open-three-phase fault. Besides, the design of switching tables for machines having a number of phases higher than six becomes very complicated.

The main alternative to the VSD approach is the multi-stator (MS) modeling, which is particularly suitable for multi-three-phase machines. The MS approach models the machine as multiple three-phase sets interacting with each other and with the rotor [2], [7], [24]. In this way, the modularity of the energy production is preserved since, for each three-phase set, a dedicated (d,q) subspace is defined. Therefore, compared to the VSD, the MS-based control schemes allow easy reconfiguration of the drive after the open-phase fault. Indeed, together with the conventional FOC algorithms [11], [13], [25], the literature also reports MS-based solutions performing

the control of both the flux amplitude and torque contribution of each healthy set after an open-phase fault. Most of them use the direct flux vector control (DFVC) algorithm [7], [8], [26].

The DFVC represents a competitive alternative to the DTC algorithms [10]. Indeed, pulse-width modulators (PWM) are used, overcoming the issues on the implementation of switching patterns for multiphase motor drives with a high number of phases. The advantages of the DFVC for multi-three-phase induction motor drives have been demonstrated in [8], [26], showing the high-performance in deep flux-weakening operation.

However, all the MS-based schemes are affected by significant magnetic coupling among the three-phase sets [2], causing the potential instability of the control algorithm [21]. Besides, this issue gets worse for multi-three-phase machines with a high number of sets (e.g., 3, 4). One solution consists of limiting the dynamic performance of the control loops, as in [7], [8]. In [26], the issue was solved using deadbeat controllers, while in [27], the magnetic coupling among the three-phase sets has been removed using a specific decoupling transformation, so performing a decoupled torque regulation. Nevertheless, none of these solutions can address the instability issue if performing power-sharing strategies among the sets, making mandatory the implementation of a dedicated decoupling algorithm.

The need for decoupling action is further emphasized in the MS-based DFVC schemes since the control of each set is performed in the own stator coordinates [26]. Therefore, the decoupling algorithm must also consider the angular shifts between the sets' frames, these becoming significant if performing power-sharing operations. This issue is overcome when FOC algorithms are implemented since all sets are controlled in the rotor coordinates [25]. However, the linear torque regulation of each set at the flux-weakening operation requires calibrated machine maps [28]. Conversely, the DFVC linearizes the torque regulation over the whole speed range [26], [29].

Therefore, the goal of this work is to propose a modular MS-based DFVC scheme for multi-three-phase induction motor (IM) drives. For each three-phase unit, the direct-, independent-, and decoupled- regulation of the flux amplitude and torque contribution is performed. The proposed control solution can deal with the current and voltage constraints introduced by each unit's VSI, ensuring high performance of the torque regulation in deep flux-weakening with MTPV operation (maximum load-angle). Besides, power-sharing strategies among the sets can be performed.

Therefore, compared to the existing MS-based DFVC solutions [7], [8], [26], the contributions of the paper are listed in the following.

- A new decoupling algorithm that allows power-sharing strategies among the sets without any instability issues is implemented.
- The modularity is extended to the MTPV operation, as the load-angle of each set is independently limited.

The proposed solution represents a competitive alternative to the existing FOC algorithms for multi-three-phase IM drives [12]–[15], [25]. Compared to them, the following features are introduced:

- The torque regulation of each set is linearized over the whole speed range, avoiding the implementation of additional control modules in flux-weakening.
- The power-sharing strategies among the sets are implemented straightforwardly through the torque-sharing, thanks to the modular torque control.

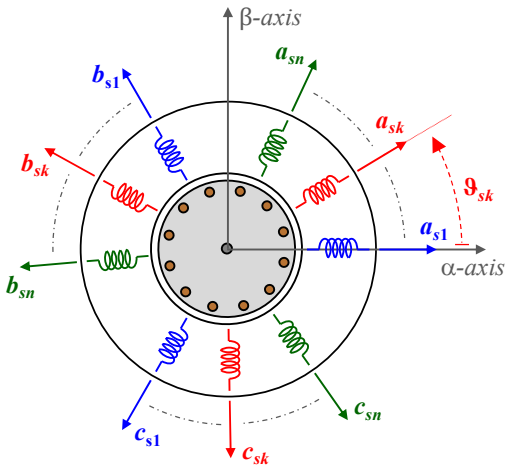

Fig. 2. Generic configuration of a multi-three-phase IM: angle displacement of the magnetic axes in one electrical revolution.

Finally, compared to the VSD-based DTC schemes [22], [23], the choice of the MS approach leads to the following advantages:

- The drive scheme can be easily configured after an open-three-phase fault.
- The VSI units use PWM three-phase modulators, allowing the control of multi-three-phase machines with a high number of sets.

The performance of the proposed solution has been validated on a twelve-phase IM prototype using a quadruple three-phase winding configuration and fed by a modular VSI.

This paper is a revised version of the work presented in [30] and includes a modular limitation of the load-angles of the sets, avoiding the machine pull-out in deep flux-weakening operation. Besides, together with the power-sharing strategies among the sets, the fault ride-through capability of the drive are demonstrated experimentally.

The paper is organized as follows. Section II reports the MS modeling of the multi-three-phase induction machine. The proposed control solution is described in Section III, while the experimental validation is given in Section IV. The paper conclusions are reported in Section V.

II. MS MODELING OF A MULTI-THREE-PHASE IM

The MS modeling aims at computing the state-space model of each set of the machine, which is essential for the design of the decoupling algorithm. In the following, a squirrel-cage IM with arbitrary numbers of pole pairs p and three-phase winding sets n is considered (Fig. 2).

A sinusoidal distribution of the stator windings is assumed, interacting with each other and with the rotor only through the spatial-fundamental component of the airgap field. The rotor cage is modeled as an equivalent three-phase winding that is sinusoidally distributed [24], [31], whose variables and parameters refer to the stator, regardless of the considered winding set. In addition, it is assumed that the stator windings have the same number of turns. Finally, iron losses are not considered.

The MS approach considers the machine as multiple three-phase sets operating in parallel, highlighting the flux and torque contributions produced by each of them [2], [24]. For each generic set k (k=1,2,…,n), the general Clarke transformation is applied [31], thus preserving the modularity of the energy conversion. Therefore, each variable defined in the k-set phase-coordinates $(abc)_k$ is computed in terms of stationary (αβ) components using the following amplitude-invariant transformation:

$$\left[T_{C,k}\right]=\frac{2}{3}\cdot\begin{bmatrix}\cos(\vartheta_{sk}) & \cos(\vartheta_{sk}+2\pi/3) & \cos(\vartheta_{sk}+4\pi/3)\\ \sin(\vartheta_{sk}) & \sin(\vartheta_{sk}+2\pi/3) & \sin(\vartheta_{sk}+4\pi/3)\end{bmatrix} \quad (1)$$

The angle ϑ_{sk} is defined as the position of the *k*-set first phase a_{sk} to the α-axis; the latter is assumed coincident with the first phase of the first set a_{s1}, a shown in Fig. 2. Therefore, MS modeling leads to *n* overlapped stationary models, and each of them can be defined in generic rotating coordinates (*xy*), using the well-known transformation [31].

A. Electromagnetic Model in Rotating Coordinates

The MS modeling of a multi-three-phase IM is analyzed in detail in [26]. In the following, the main results of [26] are reported, making easier the understanding of the proposed control solution. In summary, the electromagnetic model of a generic set *k* (*k*=1,2,…,*n*) in rotating (*xy*) coordinates is computed as:

$$\bar{v}_{sk,xy}=R_{sk}\cdot\bar{i}_{sk,xy}+\frac{d}{dt}\bar{\lambda}_{sk,xy}+j\cdot\omega_{xy}\cdot\bar{\lambda}_{sk,xy} \quad (2)$$

$$\bar{\lambda}_{sk,xy}=L_{lsk}\cdot\bar{i}_{sk,xy}+L_m\cdot\sum_{z=1}^{n}\bar{i}_{sz,xy}+L_m\cdot\bar{i}_{r,xy} \quad (3)$$

where:

- $\bar{x}_{sk,xy}=\begin{bmatrix}x_{sk,x} & x_{sk,y}\end{bmatrix}^t$ is a *k*-set vector that can assume the meaning of voltage *v*, current *i*, or flux-linkage λ;
- R_{sk} and L_{lsk} are the *k*-set parameters of resistance and leakage inductance, respectively;
- ω_{xy} is the synchronous speed of the (*xy*) frame;
- $\bar{i}_{r,xy}=\begin{bmatrix}i_{r,x} & i_{r,y}\end{bmatrix}^t$ is the rotor current vector;
- L_m is the magnetizing inductance;
- *j* is the complex operator defined as $\begin{bmatrix}0 & -1\\ 1 & 0\end{bmatrix}$.

All the stator sets interact with the rotor cage, modeled as an equivalent three-phase winding, and whose equations are computed as [26]:

$$\begin{bmatrix}0 & 0\end{bmatrix}^t=R_r\cdot\bar{i}_{r,xy}+\frac{d}{dt}\bar{\lambda}_{r,xy}+j\cdot(\omega_{xy}-\omega_e)\cdot\bar{\lambda}_{r,xy} \quad (4)$$

$$\bar{\lambda}_{r,xy}=L_{lr}\cdot\bar{i}_{r,xy}+L_m\cdot\sum_{z=1}^{n}\bar{i}_{sz,xy}+L_m\cdot\bar{i}_{r,xy} \quad (5)$$

where:

- R_r and L_{lr} are the rotor parameters of resistance and leakage inductance, respectively;
- $\bar{\lambda}_{r,xy}=\begin{bmatrix}\lambda_{r,x} & \lambda_{r,y}\end{bmatrix}^t$ is the rotor flux linkage vector;
- ω_e is the electrical speed of the rotor, computed as *p* times that the mechanical ω_m.

For a rotor cage, the equivalent three-phase currents cannot be measured or directly controlled. Therefore, the currents-to-fluxes relationships (3) and (5) are combined in a single vector equation as:

$$\bar{\lambda}_{sk,xy}=k_r\cdot\bar{\lambda}_{r,xy}+L_{lsk}\cdot\bar{i}_{sk,xy}+k_r\cdot L_{lr}\cdot\sum_{z=1}^{n}\bar{i}_{sz,xy} \quad (6)$$

where $k_r=L_m/(L_m+L_{lr})$ stands for the rotor coupling factor.

Finally, by performing the power balance of the machine, the *k*-set torque contribution T_k is computed as [26]:

$$T_k=\frac{3}{2}\cdot p\cdot\left(\bar{\lambda}_{sk,xy}\wedge\bar{i}_{sk,xy}\right)=\frac{3}{2}\cdot p\cdot\left(\lambda_{sk,x}\cdot i_{sk,y}-\lambda_{sk,y}\cdot i_{sk,x}\right) \quad (7)$$

More details about the computation of (7) are reported in the Appendix.

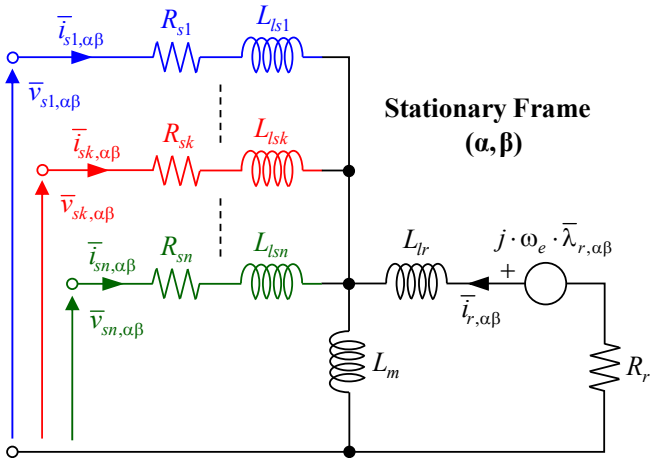

Fig. 3. Equivalent MS circuit of a generic multi-three-phase squirrel-cage IM in stationary (αβ) coordinates.

It is noted how the *k*-set torque contribution is given by the cross-product (∧) between the *k*-set flux-linkage vector and the *k*-set current vector. Further confirmation of the MS modularity is provided in Fig. 3, showing the equivalent circuit of the machine.

B. State-Space Model in Rotating Coordinates

The MS model of the machine (2)-(7) demonstrates how the coupling among the sets has a massive impact on control performance. However, the design of a modular drive scheme requires the computation of the state-space model associated with each set. Some preliminary variables are defined in (8), simplifying the interpretation of the state-space equations.

$$w_z=k_r\cdot\frac{L_{lr}}{L_{lsz}}\cdot x_{f,z}\qquad c_k=\sum_{z=1,z\neq k}^{n}w_z\qquad k_{sk}=\frac{L_m}{L_m+L_{lsk}} \quad (8)$$

The variable x_{fz} represents the status of the generic set *z* (0-faulty/1-active), thus adapting the state-space models of the healthy sets after an open-phase fault. Based on the proposed control solution, the (*xy*) components of the stator current vectors are chosen as state-space variables.

However, the state-equation of the rotor flux vector is also presented, thus reporting the complete state-space model of the machine. Such an equation is computed by combining (4) with (5) as:

$$\frac{d}{dt}\bar{\lambda}_{r,xy}=-\left[\tau_r^{-1}+j\cdot(\omega_{xy}-\omega_e)\right]\cdot\bar{\lambda}_{r,xy}+k_r\cdot R_r\cdot\sum_{z=1}^{n}\bar{i}_{sz,xy} \quad (9)$$

where $\tau_r=(L_m+L_{lr})/R_r$ is the rotor time-constant. The state-space equation of the *k*-set current vector is computed as:

$$\begin{cases}L_k\cdot\dfrac{d}{dt}i_{sk,x}=-R_k\cdot i_{sk,x}+M_k\cdot i_{sk,y}+\ldots\\ \quad\ldots+\displaystyle\sum_{z=1,z\neq k}^{n}\left(-P_z\cdot i_{sz,x}+Q_z\cdot i_{sz,y}\right)+\ldots\\ \quad\ldots+\tau_r^{-1}\cdot\lambda_{sk,x}+\omega_e\cdot\lambda_{sk,y}+F_{sk,x}\\ L_k\cdot\dfrac{d}{dt}i_{sk,y}=-M_k\cdot i_{sk,x}-R_k\cdot i_{sk,y}+\ldots\\ \quad\ldots+\displaystyle\sum_{z=1,z\neq k}^{n}\left(-Q_z\cdot i_{sz,x}-P_z\cdot i_{sz,y}\right)+\ldots\\ \quad\ldots-\omega_e\cdot\lambda_{sk,x}+\tau_r^{-1}\cdot\lambda_{sk,y}+F_{sk,y}\end{cases} \quad (10)$$

Based on (10), the following considerations for the generic set k can be made:

i) the set is characterized by an own equivalent inductance, valid for both (xy) axes, and computed as:

$$L_k = (1+c_k)\cdot L_{lsk} + k_r \cdot L_{lr} \tag{11}$$

ii) the self-coupling of the set, consisting of how the k-set currents affect their time-derivatives, depends on the following parameters:

$$\begin{aligned} R_k &= R_{sk}\cdot(1+c_k) + R_r\cdot(k_r/k_{sk}) \\ M_k &= \omega_e \cdot c_k \cdot L_{lsk} + (\omega_{xy} - \omega_e)\cdot L_k \end{aligned} \tag{12}$$

iii) each mutual coupling of the set, consisting of how the z-set currents (z=1,2,…,n, $z \neq k$) affect the time-derivatives of the k-set currents, depends on the following parameters:

$$P_z = k_r \cdot R_r - w_z \cdot R_{sz} \quad Q_z = -\omega_e \cdot w_z \cdot L_{lsz} \tag{13}$$

iv) the back-electromotive-force (back-emf) of the set depends on the k-set flux, together with the values of rotor time-constant τ_r and rotor electrical speed ω_e;

v) the time-derivatives of the k-set currents are controlled through the variables $F_{sk,x}$, and $F_{sk,y}$. These forcing terms, having the meaning of voltages, are defined as:

$$\begin{aligned} F_{sk,x} &= (1+c_k)\cdot v_{sk,x} - \sum_{z=1\div n, z\neq k}^{n} (w_z \cdot v_{sz,x}) \\ F_{sk,y} &= (1+c_k)\cdot v_{sk,y} - \sum_{z=1\div n, z\neq k}^{n} (w_z \cdot v_{sz,y}) \end{aligned} \tag{14}$$

The state-space model of the machine (2), (10) shows how the currents of each set also depend on the voltages applied by the other units (14), leading to a "voltage-coupling" phenomenon. The potential instability of the MS-based control schemes [21] is caused by this effect, making necessary the implementation of a decoupling algorithm. Otherwise, the control performance must be limited [7], [8], [21], [25], hindering the implementation of power-sharing strategies among the sets.

In the following, superscripts *, $\hat{}$, $\tilde{}$ denote a reference-, observed- and estimated- variable, respectively.

III. Modular Flux and Torque Control Scheme

The proposed control solution is designed for multi-three-phase IM drives having an arbitrary number of units n. The generic unit k (k=1,2,…,n) is controlled regardless of the others, thus considering its values of dc-link voltage $v_{dc,k}$, and amplitude limit of the phase-currents $I_{max,k}$. The current limit is usually related to the overload capability of the VSI, although in some cases, it can correspond with the thermal limit of the machine [32]. Since each winding set has an isolated neutral point (Fig. 1), the drive can be configured as modular units operating in parallel. Therefore, the generic unit k can be considered regardless of the others.

The control of the generic unit k is performed using the drive scheme proposed in Fig. 4. It corresponds to the configuration of a three-phase drive, thus requiring the measurements of the phase currents $[i_{sk,abc}]=[i_{sk\text{-}a}\ i_{sk\text{-}b}\ i_{sk\text{-}c}]^t$, dc-link voltage $v_{dc,k}$, and VSI unit status $x_{f,k}$.

In this work, a "sensored" control algorithm is proposed, thus requiring the feedback of the rotor mechanical position ϑ_m. Since a digital controller is used, the measurements above mentioned are sampled and converted in time-discrete values. In the following, the discrete samples are denoted with the superscript τ, representing the considered sample time instant.

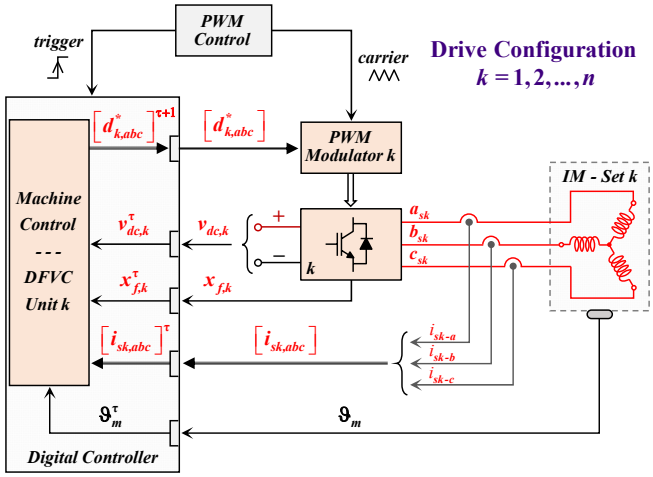

Fig. 4. Drive configuration of a generic unit k (k=1,2,…,n).

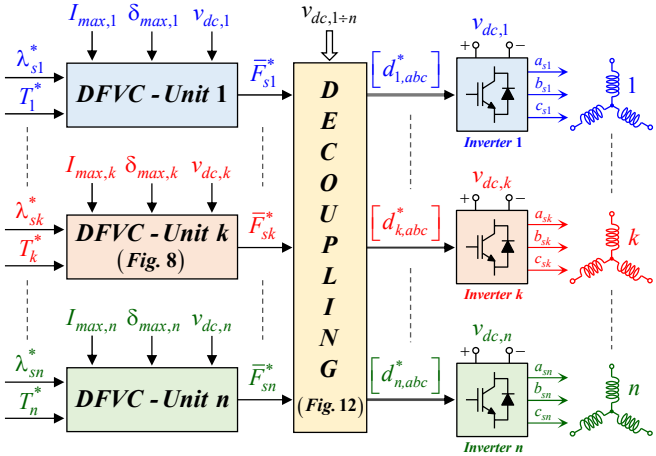

Fig. 5. Modular DFVC scheme for multi-three-phase IM drives.

Finally, the outputs of the k-unit control algorithm consist of the k-unit duty-cycles $[d^*_{k,abc}]$. Concerning Fig. 4, the duty-cycles are denoted with the superscript (τ+1) to highlight their application for the next sample time instant, thus considering the execution delay of the digital controller.

The proposed modular control scheme can perform power-sharing strategies among the sets, leading to a drive solution suitable for the "series/parallel" configurations (e.g., wind energy conversion systems) [15]. The proposed drive scheme is shown in Fig. 5, and it consists of multiple DFVC schemes operating in parallel. Therefore, the generic unit k has its references in terms of flux amplitude λ_{sk}^* and torque contribution T_k^*.

The torque reference of each set can be provided by an outer controller, not considered here since it is beyond the scope of this work. Regarding the flux amplitudes of the sets, these can be imposed different from each other if significant unbalances between the stator leakage inductances ($L_{ls,k}$) exist. Such a condition can happen if the machine has been built using an off-the-shelf stator core for three-phase motors, reducing cost [11], [33]. Apart from this case, there is no reason for keeping the flux amplitudes of the sets different from each other. A standard solution consists of using the rated flux value of the machine for all sets [7], [8]. In the alternative, the maximum-torque per ampere (MTPA) operation can be performed [34], minimizing the overall Joule losses.

As shown in Fig. 5, the k-unit DFVC performs the regulation of the k-set flux amplitude λ_{sk} and k-set torque T_k considering the limits of the k-unit VSI in terms of voltage $v_{dc,k}$ and current $I_{max,k}$.

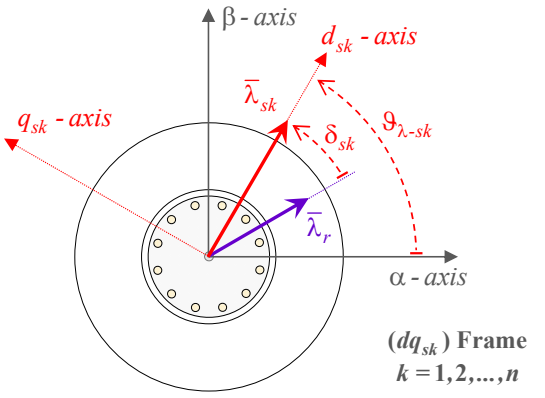

Fig. 6. Rotating k-set flux frame (dq_{sk}).

Also, the limitation of the k-set load-angle $\delta_{max,k}$ is performed, allowing the implementation of modular MTPV strategies that avoid the machine pull-out. Therefore, this angle has a similar meaning to that defined for three-phase machines [29].

The output of each DFVC scheme consists of the reference forcing term $\bar{F}_{sk}$ (k=1,2,…,n), having a similar meaning of (14). Therefore, the decoupling algorithm is applied, leading to the computation of the duty-cycles of the inverters.

All the details are provided in the next subsections, reporting a description of the proposed control solution.

A. DFVC Equations

The k-unit DFVC scheme is implemented in the rotating k-set flux-coordinates (dq_{sk}), as shown in Fig. 6. The position of the d_{sk}-axis corresponds with that of the k-set flux vector $\vartheta_{\lambda\text{-}sk}$, while the k-set load-angle δ_{sk} is defined as the position of the k-set flux vector to the rotor flux vector. Finally, the synchronous speed ω_{sk} of the (dq_{sk}) frame is defined as the speed of the d_{sk}-axis to the stationary α-axis.

Therefore, the electric- and torque- equations of the generic set k (2), (7) are computed in (dq_{sk}) coordinates as:

$$v_{sk,d_{sk}} = R_{sk} \cdot i_{sk,d_{sk}} + \frac{d}{dt}\lambda_{sk} \tag{15}$$

$$T_k = 3/2 \cdot p \cdot \lambda_{sk} \cdot i_{sk,q_{sk}} \tag{16}$$

According to (15), the k-set flux amplitude is regulated directly using the k-set d_{sk}-axis voltage component $v_{sk,d_{sk}}$, while (16) shows how the k-set torque contribution can be regulated using the k-set q_{sk}-axis current component $i_{sk,q_{sk}}$. Therefore, the DFVC of each unit performs the torque regulation through the direct control of torque-producing current component, obtaining a high level of decoupling among the (dq_{sk}) axes.

B. Stator Flux Observer

For each k-unit DFVC scheme (k=1,2,…,n), a flux-observer is implemented, obtaining the amplitude λ_{sk} and the position $\vartheta_{\lambda\text{-}sk}$ of the k-set flux vector. The k-unit observer structure is shown in Fig. 7. It consists of a reduced-order observer [35] to keep the modularity of the proposed control solution.

The k-unit observer is obtained as a combination of two model-based estimators, both implemented in stationary (αβ) coordinates. At high speed, the observer is based on back-emf integration (*Voltage Model - VI*). Conversely, the low-speed operation is based on the k-set current-to-flux relationships (*Current Model - Iϑ*).

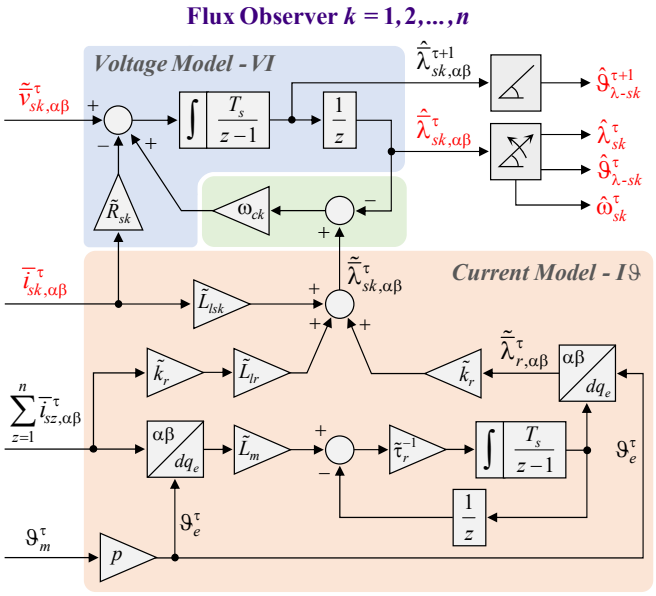

Fig. 7. Flux observer of a generic unit k (k=1,2,…,n).

The *Current Model - Iϑ* estimates the k-set flux vector using the k-set magnetic equation (6). The rotor flux vector is estimated by implementing (9) in rotor electrical coordinates (dq_e), making necessary the computation of the electrical angle ϑ_e from that mechanical ϑ_m (Fig. 7). Since the k-set flux estimation does not require the reconstruction of the k-set phase-voltages, the *Current Model - Iϑ* is immune to the dead-time (DT) voltage errors introduced by the k-unit VSI.

The *Voltage Model - VI* performs the estimation of the k-set flux vector through the Euler integration of the k-set electric equation (2). The estimation of the DT errors is recommended, allowing an accurate reconstruction of the k-set voltages [36]. The *Voltage Model - VI* guarantees high observation performance in both medium- and high- speed ranges of the machine, resulting in robust against detuning errors of the machine parameters (e.g., stator resistance). Besides, due to the execution delay of the digital controller, the Euler integration of the k-set back-emf corresponds to the k-set flux vector for the next sample time instant (τ+1). Therefore, the predicted position of the (dq_{sk}) frame is computed (Fig. 7) since its use allows full stability of the control scheme in the high-speed operation of the machine, as shown in the next subsections.

The transition frequency (rad/s) between the two estimators corresponds to the observer gain $\omega_{c,k}$, as the transfer function of the k-unit flux observer is computed as:

$$\hat{\bar{\lambda}}_{sk,\alpha\beta} = \tilde{\bar{\lambda}}_{sk,\alpha\beta} \cdot \frac{\omega_{ck}}{\omega_{ck} + \mathcal{L}} + \left(\frac{\tilde{\bar{v}}_{sk,\alpha\beta} - R_s \cdot \bar{i}_{sk,\alpha\beta}}{\mathcal{L}} \right) \cdot \frac{\mathcal{L}}{\mathcal{L} + \omega_{ck}} \tag{17}$$

where $\mathcal{L}$ is the Laplace variable. According to (17), the flux estimate obtained with the *Current Model - Iϑ* (6) corresponds with the observer output when the synchronous speed of the machine is lower than the transition frequency $\omega_{c,k}$ (rad/s). Conversely, the back-emf integration, consisting of the flux estimate obtained with the *Voltage Model - VI*, prevails when the synchronous speed of the IM is higher than $\omega_{c,k}$. The design procedure of the observer gain is reported in [35].

In this work, the value of $\omega_{c,k}$ = 125 rad/s (20 Hz), has been chosen for all units (k=1,2,3,4), obtaining a good dynamic performance.

Finally, the components of the k-set flux vector are used to compute the related values of amplitude λ_{sk}, position $\vartheta_{\lambda\text{-}sk}$, and synchronous speed ω_{sk}, as shown in Fig. 7.

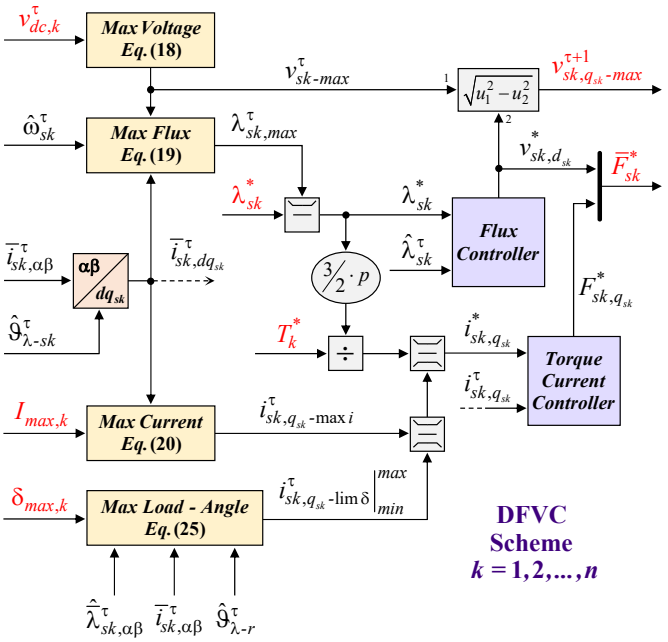

Fig. 8. DFVC scheme of a generic unit *k*.

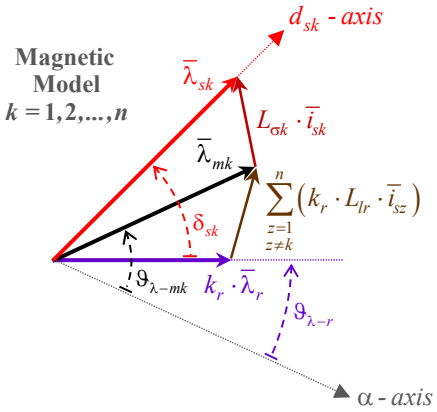

Fig. 9. Vector diagram of the *k*-set magnetic model.

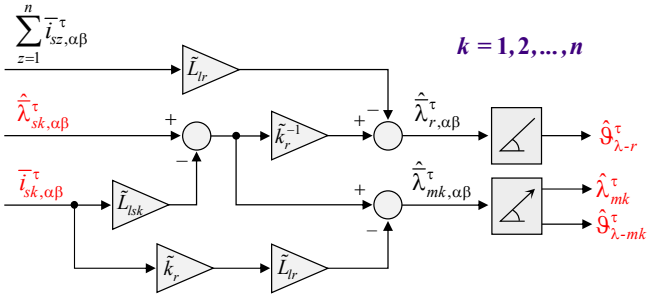

Fig. 10. Execution scheme for computing the *k*-set magnetizing flux vector and the position of the rotor flux vector.

C. DFVC Scheme

The DFVC scheme of a generic unit *k* is shown in Fig. 8. The primary inputs of the *k*-unit DFVC scheme are the references of *k*-set flux amplitude λ_{sk}^* and *k*-set torque contribution T_k^* (Fig. 5).

Besides, the *k*-unit constraints in terms of dc-link voltage $v_{dc,k}$, and amplitude limit of the phase-currents $I_{max,k}$ are considered. Finally, the limitation of the *k*-set load-angle $\delta_{max,k}$ is included.

Therefore, after computing the *k*-set currents in (dq_{sk}) coordinates (Fig. 8), the following actions are performed:

1) Flux amplitude limitation
2) Torque-producing current limitation
3) Load-angle limitation
4) Flux and torque-producing current regulations

1) Flux amplitude limitation

The voltage control of the *k*-unit VSI is performed using a PWM three-phase modulator, allowing the adoption of the well-known modulation techniques [37]. Therefore, the amplitude limit of the *k*-unit phase-voltages is computed as:

$$v_{sk\text{-}max}^{\tau} = v_{dc,k}^{\tau} \Big/ \sqrt{3} \tag{18}$$

The *k*-unit voltage limit (18) is then combined with the *k*-set electric equation (2) computed in (dq_{sk}) coordinates, obtaining to the limit of the *k*-set flux amplitude reference:

$$\lambda_{sk}^* < \lambda_{sk\text{-}max}^{\tau} \cong \frac{v_{sk\text{-}max}^{\tau} - \tilde{R}_{sk} \cdot i_{sk,q_{sk}}^{\tau} \cdot sign\left(\hat{\omega}_{sk}\right)}{\hat{\omega}_{sk}^{\tau}} \tag{19}$$

In this way, a model-based flux-weakening law is implemented, avoiding the use of an outer voltage controller.

Based on (16), the *k*-set flux amplitude reference λ_{sk}^*, together with the *k*-set reference torque T_k^*, defines the reference of the *k*-set torque-producing current $i_{sk,q_{sk}}^*$ (Fig. 8).

2) Torque-producing current limitation

The reference of the *k*-set torque-producing current must be limited to respect the amplitude limit of the *k*-unit phase-currents $I_{max,k}$. Therefore, according to the *k*-unit d_{sk}-axis current, the following saturation limit is computed:

$$i_{sk,q_{sk}\text{-}\max i}^{\tau} = \sqrt{I_{max,k}^{\ 2} - i_{sk,d_{sk}}^{\tau\ 2}} \tag{20}$$

This limitation is applied regardless of the sign of the *k*-set torque-producing current reference, as shown in Fig. 8.

3) Load-angle limitation

The DFVC scheme for three-phase drives limits the machine load-angle through an outer controller [29], thus considering all the magnetic non-linearities. However, this solution requires tricky tuning procedures and does not guarantee high control performance in deep flux-weakening. For this reason, this work proposes the limitation of the *k*-set load-angle using a model-based regulation law. In this way, no outer controllers are implemented, reducing the complexity of the control algorithm.

The *k*-set magnetic equation (6) in (dq_{sk}) coordinates is considered, expressed in the following form:

$$\bar{\lambda}_{sk,dq_{sk}} = \bar{\lambda}_{mk,dq_{sk}} + L_{\sigma k} \cdot \bar{i}_{sk,dq_{sk}} \tag{21}$$

where the *k*-set magnetizing flux vector $\bar{\lambda}_{mk,dq_{sk}}$ and the *k*-set overall leakage inductance $L_{\sigma k}$ are defined as:

$$\begin{aligned} \bar{\lambda}_{mk,dq_{sk}} &= k_r \cdot \bar{\lambda}_{r,dq_{sk}} + \sum_{z=1,z\neq k}^{n} \left(k_r \cdot L_{lr} \cdot \bar{i}_{sz,dq_{sk}}\right) \\ L_{\sigma k} &= L_{lsk} + k_r \cdot L_{lr} \end{aligned} \tag{22}$$

The vector diagram of (21) is depicted in Fig. 9, highlighting the relationship between the *k*-set current vector and the *k*-set load-angle δ_{sk}. After performing some geometrical considerations, the following equation is computed:

$$i_{sk,q_{sk}} = \frac{\lambda_{mk}}{L_{\sigma k}} \cdot \sin\left(\delta_{sk} - \vartheta_{\lambda-mk} + \vartheta_{\lambda-r}\right) \tag{23}$$

where the amplitude λ_{mk} and position $\vartheta_{\lambda\text{-}mk}$ of the *k*-set magnetizing flux vector (21), (22), and the position of the rotor flux vector $\vartheta_{\lambda\text{-}r}$ are computed using the execution scheme shown in Fig. 10.

The limitation of the k-set load-angle is performed regardless of the sign of the latter. Therefore, based on the k-set load-angle limit $\delta_{max,k}$, the following regulation law is implemented (Fig. 8):

$$i^{\tau}_{sk,q_{sk}-\lim\delta}\Big|_{min} \le i^{*}_{sk,q_{sk}} \le i^{\tau}_{sk,q_{sk}-\lim\delta}\Big|^{max} \tag{24}$$

where the saturation limits are computed as:

$$\begin{aligned} i^{\tau}_{sk,q_{sk}-\lim\delta}\Big|_{min} &= \frac{\hat{\lambda}^{\tau}_{mk}}{\tilde{L}_{\sigma k}} \cdot \sin\left(-\delta_{max,k} - \hat{\vartheta}^{\tau}_{\lambda-mk} + \hat{\vartheta}^{\tau}_{\lambda-r}\right) \\ i^{\tau}_{sk,q_{sk}-\lim\delta}\Big|^{max} &= \frac{\hat{\lambda}^{\tau}_{mk}}{\tilde{L}_{\sigma k}} \cdot \sin\left(\delta_{max,k} - \hat{\vartheta}^{\tau}_{\lambda-mk} + \hat{\vartheta}^{\tau}_{\lambda-r}\right) \end{aligned} \tag{25}$$

The proposed solution allows at setting arbitrary values of the k-set load-angle limit $\delta_{max,k}$, obtaining the maximum degree of modularity in the control of each unit, and representing an absolute novelty over the existing literature. If this limit is set at 45 electrical degrees for all sets, modular MTPV strategies that avoid the machine pull-out are performed.

4) Flux and torque-producing current regulations

The k-unit control consists of the regulation of the k-unit stator flux amplitude and the k-unit torque-producing current, using proportional-integral (PI) controllers (Fig. 8).

The k-set flux amplitude can be directly regulated using the k-unit d_{sk}-axis voltage component (15), without requiring any decoupling action. Besides, based on the k-unit voltage limit (18), the operative range $v^{\tau+1}_{sk,q_{sk}-max}$ of the k-unit q_{sk}-axis voltage component is computed, as shown in Fig. 8.

The k-unit torque-producing current controller must be designed according to the state-space equation (10) computed in (dq_{sk}) coordinates. In detail, the q_{sk}-axis component is considered, obtaining the following equation:

$$\begin{aligned} L_k \cdot \frac{d}{dt} i_{sk,q_{sk}} &= -M_k \cdot i_{sk,d_{sk}} - R_k \cdot i_{sk,q_{sk}} + \dots \\ \dots &+ \sum_{z=1,z\neq k}^{n} \left(-Q_z \cdot i_{sz,d_{sk}} - P_z \cdot i_{sz,q_{sk}}\right) - \omega_e \cdot \lambda_{sk} + F_{sk,q_{sk}} \end{aligned} \tag{26}$$

The voltage coupling among the sets is noted. Therefore, the output of the k-unit torque-producing current controller should not be considered as the k-unit q_{sk}-axis reference voltage. Otherwise, significant conflicts with the controllers of the other units arise, leading to the potential instability of the control scheme [21].

In this work, the instability issue is solved by considering the output of each torque-producing current controller as a linear combination of the voltage references belonging to all units. Referring to (14), this combination is defined as:

$$F^{*}_{sk,q_{sk}} = (1+c_k) \cdot v^{*}_{sk,q_{sk}} - \sum_{z=1,z\neq k}^{n} \left(w_z \cdot v^{*}_{sz,q_{sk}}\right) \tag{27}$$

Regarding the design of the k-unit controller gains, the same tuning procedures of the DFVC scheme for three-phase drives can be adopted, considering the k-set parameters of inductance (11) and resistance (12). Besides, the performance can be further improved if the mutual couplings among the sets (13) are compensated, using dedicated feed-forwards. Indeed, the current-couplings act as additive disturbances that are in any case compensated by the q_{sk}-axis current controller.

D. Voltage Decoupling Algorithm

The output of the k-unit torque-producing current control consists of a reference combination of all units' voltages, evaluated along the q_{sk}-axis.

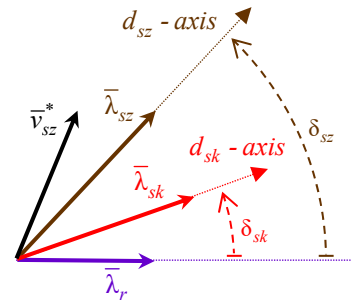

Fig. 11. Rotating frames of the generic units k and z.

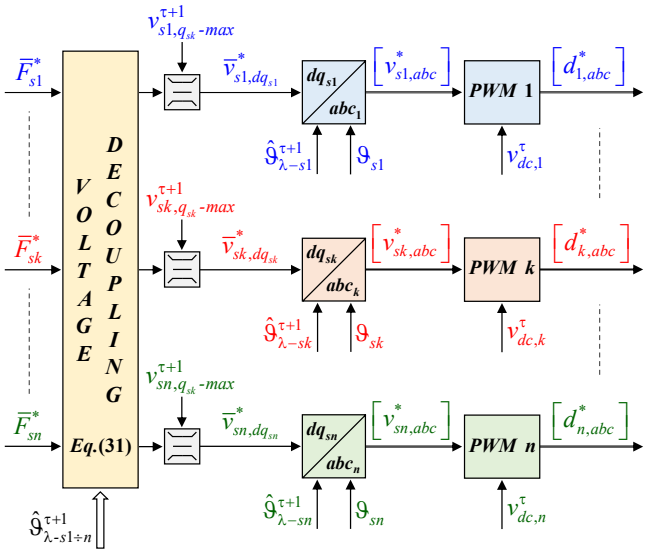

Fig. 12. Computation of the duty-cycles for the VSI units.

Therefore, a decoupling algorithm to extrapolate the k-unit q_{sk}-axis reference voltage must be implemented. Compared to [26], the proposed decoupling solution can consider load-angle values of the sets different from each other, allowing the implementation of torque-sharing strategies.

Two generic unit k and z are initially considered. Based on the vector diagram shown in Fig. 11, the z-unit reference voltage along the q_{sk}-axis can be expressed in terms of (dq_{sz}) coordinates as:

$$v^{*}_{sz,q_{sk}} = \sin\left(\delta^{\tau+1}_{sz} - \delta^{\tau+1}_{sk}\right) \cdot v^{*}_{sz,d_{sz}} + \cos\left(\delta^{\tau+1}_{sz} - \delta^{\tau+1}_{sk}\right) \cdot v^{*}_{sz,q_{sz}} \tag{28}$$

Therefore, by replacing (28) in (27), the following equation is obtained:

$$C^{*}_{sk,q_{sk}} = (1+c_k) \cdot v^{*}_{sk,q_{sk}} - \sum_{z=1,z\neq k}^{n} \left[w_z \cdot v^{*}_{sz,q_{sz}} \cdot \cos\left(\delta^{\tau+1}_{sz} - \delta^{\tau+1}_{sk}\right)\right] \tag{29}$$

where all the known components have been grouped as:

$$C^{*}_{sk,q_{sk}} = F^{*}_{sk,q_{sk}} + \sum_{z=1,z\neq k}^{n} \left[w_z \cdot v^{*}_{sz,d_{sz}} \cdot \sin\left(\delta^{\tau+1}_{sz} - \delta^{\tau+1}_{sk}\right)\right] \tag{30}$$

By merging (29) for all sets (k=1,2,…,n), and after performing several mathematical manipulations, the k-unit q_{sk}-axis reference voltage is extrapolated as follows:

$$v^{*}_{sk,q_{sk}} = s^{\tau+1}_{(k,k)} \cdot C^{*}_{sk,q_{sk}} + \sum_{z=1,z\neq k}^{n} \left(s^{\tau+1}_{(k,z)} \cdot C^{*}_{sz,q_{sz}}\right) \tag{31}$$

More details about the decoupling equation (31) are reported in the Appendix, together with the description of the decoupling coefficients $s_{(k,k)}$, $s_{(k,z)}$. Using (31), the reference voltages combination required by each DFVC scheme is satisfied, ensuring the direct and decoupled control of each set.

Besides, since the coefficients of (31) consider the status of each unit (8), the proposed decoupling algorithm is automatically configured after an open-three-phase fault. Finally, the k-unit q_{sk}-axis reference voltage could be limited to the value $v_{sk,q_{sk}-max}^{\tau+1}$ (Fig. 12), thus respecting the k-unit voltage limit (18).

Once the k-unit reference voltages in (dq_{sk}) coordinates are obtained, the inverse rotational- and Clarke- transformations (1) are applied, as shown in Fig. 12. However, to consider the application of the reference voltages in the next sample time instant (τ+1), the predicted position of the (dq_{sk}) frame is used (Fig. 7). In this way, the execution delay of the digital controller is fully compensated, allowing high control performance over the whole speed range of the machine.

E. Pulse-Width Modulation

The VSI of each unit has its own PWM modulator, performing the energy conversion at a constant switching frequency. Therefore, starting from the k-unit reference voltages in $(abc)_k$ coordinates $[v_{sk,abc}^{*}]$, the k-unit duty-cycles $[d_{k,abc}^{*}]$ are computed using the three-phase modulation techniques [37], [38], as shown in Fig. 12. In this work, the "MinMax" modulation has been implemented for all units.

IV. Experimental Validation

The proposed control solution has been validated on a twelve-phase asymmetrical IM (Fig. 13), rated 10 kW at 200 Hz (4 poles). The stator consists of four sets using full-pitch, 1 slot/phase/pole windings, obtaining a quadruple-three-phase configuration [39]. The magnetic phase-shift between two consecutive sets is 15 electrical degrees, as shown in Fig. 14. The winding sets have identical stator parameters, as shown in Table I, listing the primary machine data. The coupling coefficients (8) and the parameters of the state-space model (10) are reported in Table II and Table III, respectively.

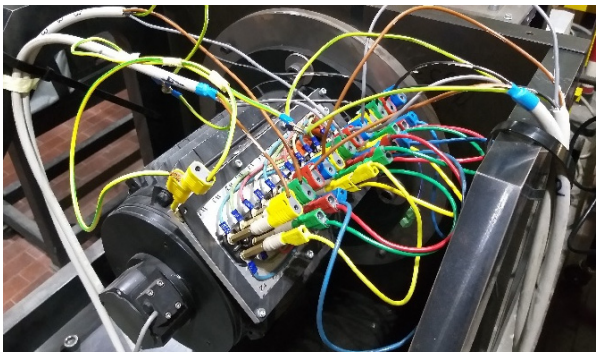

Fig. 13. Twelve-phase IM prototype.

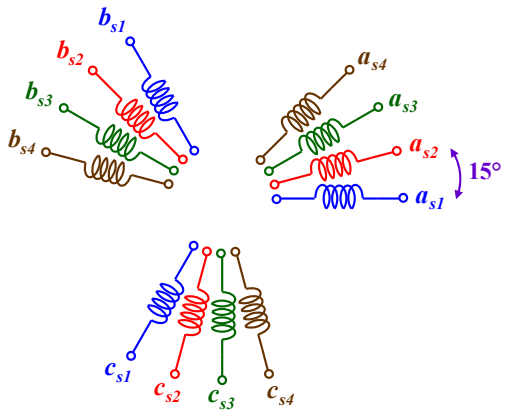

Fig. 14. Asymmetrical quadruple-three-phase winding configuration.

TABLE I. Data of the Machine Under Test

Electrical Data	
Phase number	12 (n = 4)
Pole pairs p	2
Rated power $P_{m,rated}$	10 kW
Rated phase-voltage	115 V (rms)
Rated current	10 A (rms)
Rated frequency	200 Hz
Machine Parameters	
Stator resistance R_{sk} (k=1,2,3,4)	145 mΩ
Stator leakage inductance L_{lsk} (k=1,2,3,4)	940 μH
Rated magnetizing inductance $L_{m,rated}$	4.3 mH
Rotor resistance R_r	45 mΩ
Rotor leakage inductance L_{lr}	235 μH
Stator coupling factor k_{sk} (k=1,2,3,4)	0.821
Rotor coupling factor k_r	0.948
Overall leakage inductance $L_{\sigma k}$ (k=1,2,3,4)	1.16 mH
Rated stator flux amplitude $\lambda_{s,rated}$	115 mVs

TABLE II. Coupling Coefficients of the Winding Sets

Single set coefficient w_z	
Unit z ON ($x_{f,z}$ = 1)	0.237
Unit z OFF ($x_{f,z}$ = 0)	0
Coupling coefficient c_k – Unit k ON ($x_{f,k}$ = 1)	
4 units ON ($x_{f,z}$ = 1, z =1,2,3,4)	0.711
3 units ON	0.474
2 units ON	0.237
Only unit k ON ($x_{f,z}$ = 0, $z \neq k$)	0

TABLE III. Parameters of the K-Set State-Space Model

Equivalent inductance L_k – Unit k ON ($x_{f,k}$ = 1)	
4 units ON ($x_{f,z}$ = 1, z =1,2,3,4)	1.83 mH
3 units ON	1.61 mH
2 units ON	1.39 mH
Only unit k ON ($x_{f,z}$ = 0, $z \neq k$)	1.16 mH
Equivalent resistance R_k – Unit k ON ($x_{f,k}$ = 1)	
4 units ON ($x_{f,z}$ = 1, z =1,2,3,4)	300 mΩ
3 units ON	266 mΩ
2 units ON	231 mΩ
Only unit k ON ($x_{f,z}$ = 0, $z \neq k$)	197 mΩ
Equivalent mutual reactance M_k – Unit k ON ($x_{f,k}$ = 1)	
4 units ON ($x_{f,z}$ = 1, z =1,2,3,4)	$(1.83 \cdot \omega_{xy} - 1.16 \cdot \omega_e)$ mΩ
3 units ON	$(1.61 \cdot \omega_{xy} - 1.16 \cdot \omega_e)$ mΩ
2 units ON	$(1.39 \cdot \omega_{xy} - 1.16 \cdot \omega_e)$ mΩ
Only unit k ON ($x_{f,z}$ = 0, $z \neq k$)	$(1.16 \cdot \omega_{xy} - 1.16 \cdot \omega_e)$ mΩ
Mutual resistance of set k due to set z ($z \neq k$) P_z	
Unit z ON ($x_{f,z}$ = 1)	8.3 mΩ
Unit z OFF ($x_{f,z}$ = 0)	0 mΩ
Mutual reactance of set k due to set z ($z \neq k$) Q_z	
Unit z ON ($x_{f,z}$ = 1)	$(-0.22 \cdot \omega_e)$ mΩ
Unit z OFF ($x_{f,z}$ = 0)	0 mΩ

A. Test Rig

The machine has been mounted on a test rig for validation purposes. The rotor shaft has been coupled to a driving machine acting as a prime mover, as shown in Fig. 15. Due to the mechanical limitations of the test rig, the machine speed has been limited at 6000 r/m. The rotor mechanical position has been measured with an incremental encoder having a resolution of 1024 pulses/r.

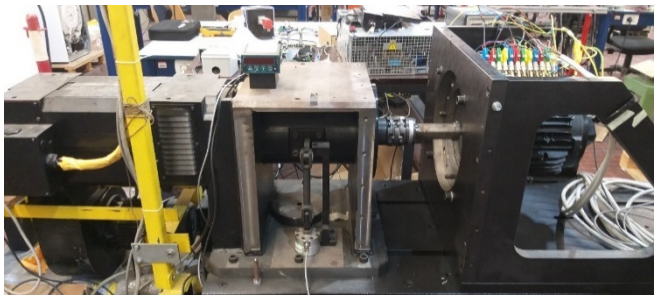

Fig. 15. View of the machine under test (right) and driving machine (left).

The power converter consists of custom-made power electronics building blocks (PEBBs) [40]. Each of these is a three-phase VSI based on the insulated-gate bipolar transistor (IGBT) modules (100 A, 1200 V). The VSIs are fed by a single dc source at 270 V. The switching frequency has been set at 4 kHz (dead-time of 1.5 µs), providing a scenario that is compatible with the industrial implementations.

The digital controller is the dSPACE® DS1103 PPC Controller Board, using 4 kHz of sampling frequency (single-edge PWM modulation). The control algorithm has been developed in the C-code environment.

B. *Experimental Results*

The experimental results are provided for the drive operation with both torque and speed control modes. The latter has been implemented using an outer PI controller, which provides the machine reference torque T^*, while the driving machine behaves an inertial load. The balanced operation of the sets has been preliminarily tested, followed by the execution of the torque-sharing strategies. Experimental results are provided for the following tests:

1) Torque control in generation mode
2) Torque reversal
3) Fault ride-through capability
4) MTPV operation at deep flux-weakening
5) Steady-state torque-sharing
6) Sinusoidal torque-sharing

The dc-link voltage has been reduced at 100 V for the tests 4) and 6). In this way, the flux-weakening operation with MTPV has been performed below the speed limit of the test rig. Finally, the amplitude limit of the units' phase-currents has been set at $I_{max,k}$ = 24 A (k=1,2,3,4), allowing a machine overload torque of 200 %.

1) Torque in generation mode

The machine speed has been set at -6000 r/m, while the flux reference of the units has been set at the rated value (115 mVs). The no-load condition has been initially tested. From a specific time instant onwards, the fast torque transient (10 Nm/ms) from 0 to + 24 Nm (150 % of the rated torque in generation mode) has been performed, obtaining the results shown in Figs. 16 – 17.

Due to some asymmetries introduced from the process of machine manufacturing, the currents of the set 2 are more distorted compared to those of the other units. However, the decoupling algorithm mitigates this phenomenon without significant issues, as confirmed by Fig. 17.

The benefits of the proposed decoupling algorithm are highlighted by showing the results obtained with the conventional MS-based DFVC, whose execution scheme is shown in Fig. 18. Here, the output of the k-unit torque current controller is set equal to the q_{sk}-axis reference voltage of the unit k, thus avoiding the implementation of the decoupling algorithm (Fig. 12).

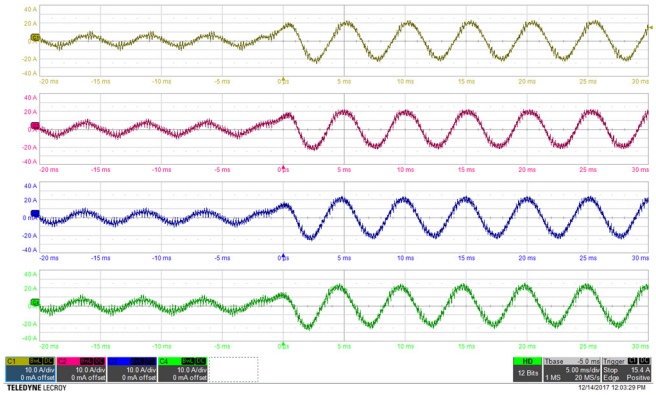

Fig. 16. Fast torque transient from no-load up to 150 % of the rated torque in the generation, at -6000 r/m. Ch1: $i_{s1\text{-}a}$ (10 A/div), Ch2: $i_{s2\text{-}a}$ (10 A/div), Ch3: $i_{s3\text{-}a}$ (10 A/div), Ch4: $i_{s4\text{-}a}$ (10 A/div). Time resolution: 5 ms/div.

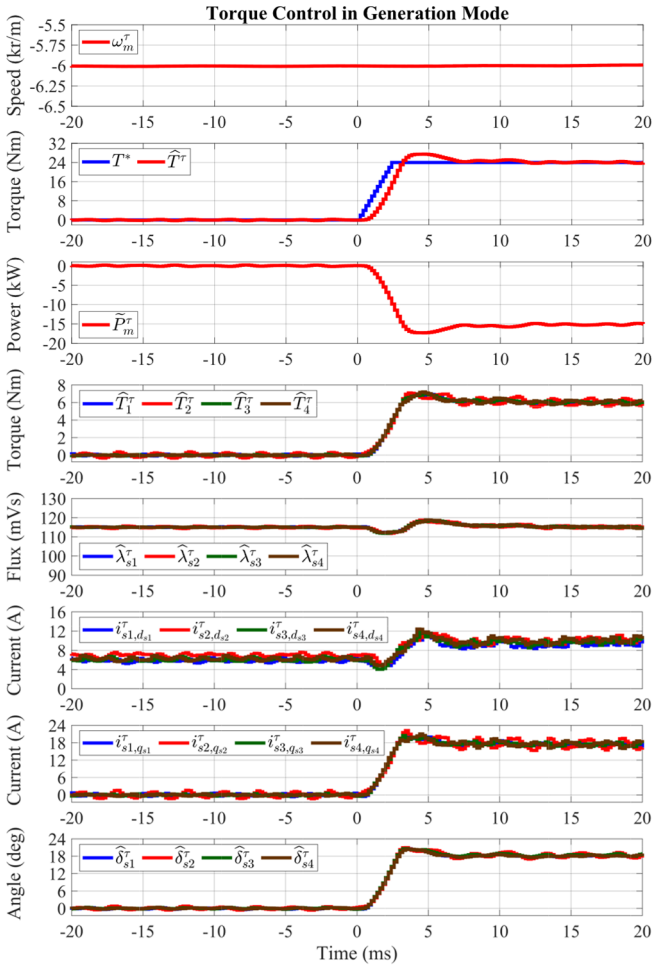

Fig. 17. Fast torque transient from no-load up to 150 % of the rated torque in the generation, at -6000 r/m.

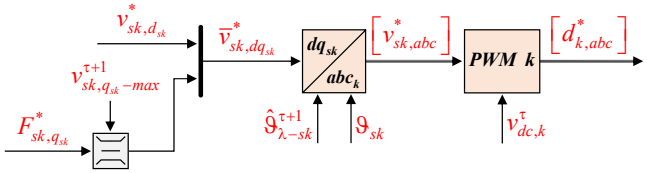

Fig. 18. Conventional MS-based DFVC scheme: the output of the k-unit torque controller is considered as the q_{sk}-axis reference voltage of the unit k.

The phase-currents waveforms obtained with this control approach have been presented in [7], and shown here in Fig. 19. It is noted how the phase-currents of unit 2 are not sinusoidal.

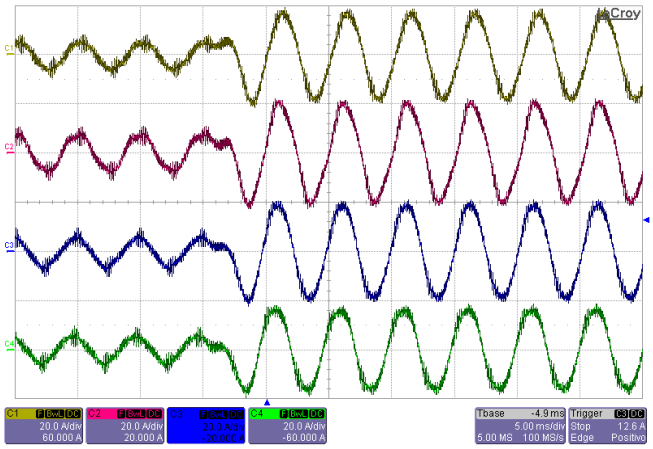

Fig. 19. Phase-currents obtained by performing test 1) with the conventional MS-based DFVC scheme [7]. Ch1: $i_{s1\text{-}a}$ (20 A/div), Ch2: $i_{s2\text{-}a}$ (20 A/div), Ch3: $i_{s3\text{-}a}$ (20 A/div), Ch4: $i_{s4\text{-}a}$ (20 A/div). Time resolution: 5 ms/div.

Also, unbalances among the sets are noted since the amplitudes of the phase-currents are significantly different from each other. Compared to results obtained with the implementation of the decoupling algorithm (Fig. 16), a significant derating in the quality of the waveforms in no-load conditions is noted too. Finally, it is highlighted that such results were obtained by limiting the dynamic performance of the control loops, avoiding instability [21].

2) Torque reversal

The machine speed has been kept at -6000 r/m. The fast torque reversal (10 Nm/ms) from – 24 Nm to + 24 Nm (150 % of the rated torque) has been performed, obtaining the results of Fig. 20. Like the previous test, the flux reference of the units has been set at the rated value (115 mVs).

In the motoring mode, the drive has operated under both the voltage and current constraints of the units. Indeed, the flux amplitudes have been controlled at a value of about 110 mVs. Besides, the torque produced by each set has not satisfied the target (- 6 Nm), as zoomed in Fig. 21. However, in the generation mode, the voltages limit of the units has not been reached. Therefore, the DFVC scheme of each unit has been able to increase the flux amplitude of its set, allowing the satisfaction of the reference torque (6 Nm).

Finally, it is noted the fast torque response of all units since the reversal has been performed in just 5 ms using only 4 kHz of switching/sampling frequency.

3) Fault ride-through capability

The drive has been operated with inverter 2 already turned-off. The same settings of the previous test in terms of machine speed and flux references have been used. The torque has been controlled at 10 Nm. From a specific time instant onwards, the inverter 3 has been turned-off, emulating the fault of a power module. The experimental results are shown in Figs. 22 – 23.

It is noted how the healthy units exhibit sinusoidal currents (Fig. 22) that must increase to keep the machine torque constant. The healthy units compensate for the torque loss caused by the shut-off of the inverter 3 in about 3 ms. The torque-producing currents of the healthy sets exhibit a slight overshoot due to the turn-off dynamic of the inverter 3. This effect also causes a temporary increase in machine torque T, as shown in Fig. 23.

Finally, thanks to the application of the decoupling algorithm, the current waveforms are less distorted than those obtained with the conventional MS-based DFVC scheme [7], as demonstrated in Fig. 24.

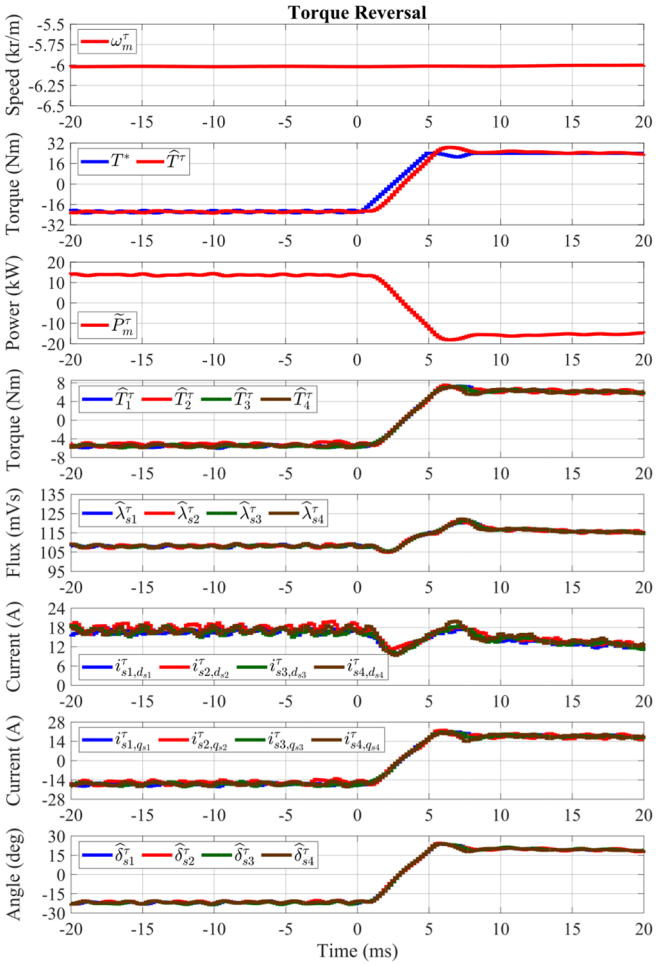

Fig. 20. Torque reversal from 150 % rated torque in motoring to 150 % rated torque in the generation, at -6000 r/m.

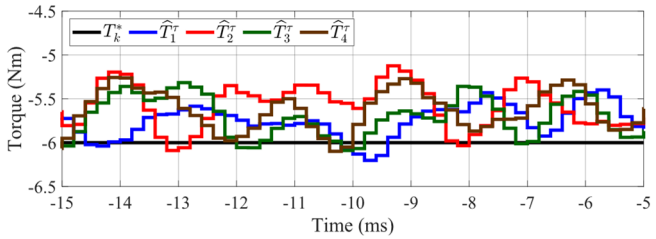

Fig. 21. Torque reversal from 150 % rated torque in motoring to 150 % rated torque in the generation, at -6000 r/m. Magnification of Fig. 20.

4) MTPV operation at deep flux-weakening

The deep flux-weakening operation with MTPV has been tested in closed-loop speed operation, and by reducing the dc-link voltage (100 V) of the inverters. The flux references of the DFVC units have been set at the MTPA limit (154 mVs) [34], allowing at reaching the maximum machine torque (32 Nm – 200 % overload).

The experimental results for a step speed-reference from 0 to 6000 r/m are shown in Fig. 25. Below the base speed, the torque limit of each set (8 Nm) depends only on the related inverter current limit (24 A).

The flux-weakening operation starts at a speed of about 1200 r/m, thus testing the quasi-constant power range of the machine [41]. The MTPV operation corresponds to the reaching of the load-angle limit for all sets. For safety, this limit has been set at 40 electric degrees ($\delta_{max,k}$, k=1,2,3,4) instead of the theoretical 45, avoid the machine pull-out.

The MTPV operation starts at a speed of about 2300 r/m, thus testing the decreasing-power range of the machine [41].

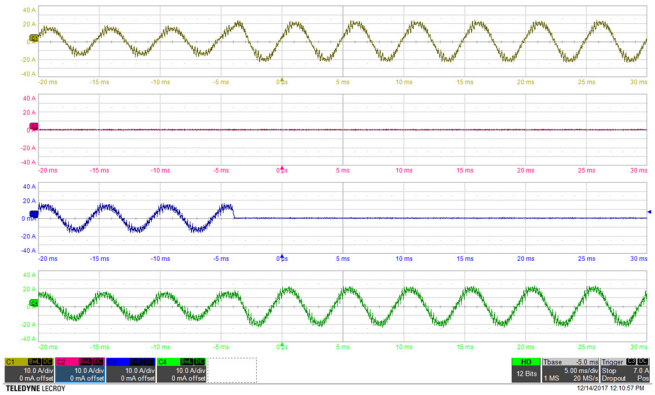

Fig. 22. Shut-off of unit 3 with unit 2 already OFF at -6000 r/m with 10 Nm. Ch1: $i_{s1\text{-}a}$ (10 A/div), Ch2: $i_{s2\text{-}a}$ (10 A/div), Ch3: $i_{s3\text{-}a}$ (10 A/div), Ch4: $i_{s4\text{-}a}$ (10 A/div). Time resolution: 5 ms/div.

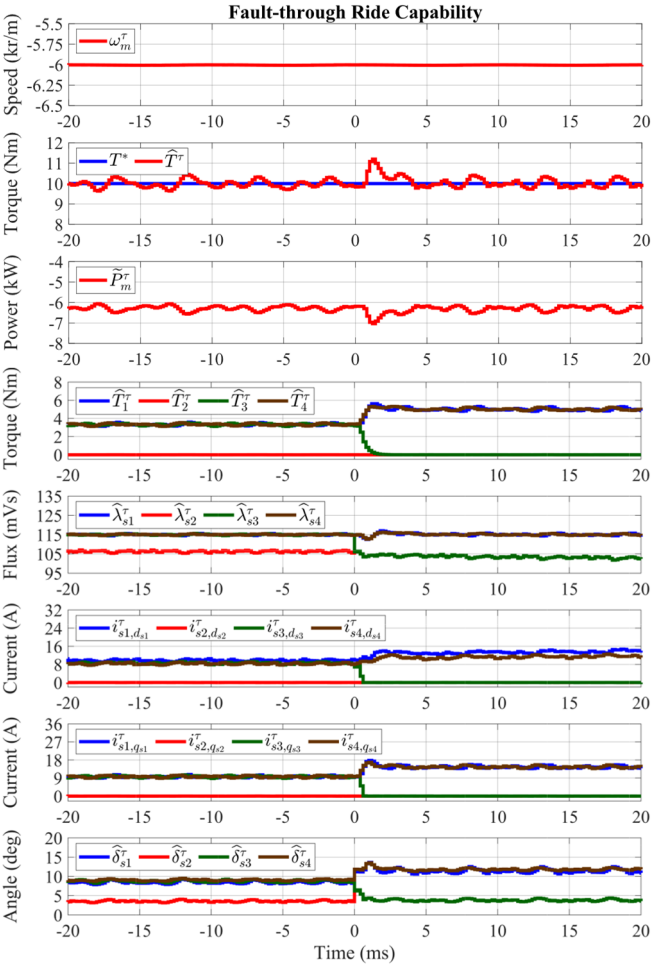

Fig. 23. Shut-off of unit 3 with unit 2 already OFF at -6000 r/m with 10 Nm.

Despite the high flux-weakening ratio (about 1/5), both the flux amplitude and load-angle values of each set are appropriately limited. Therefore, through this test, the maximum-torque per speed has been obtained, validating the machine controllability over the whole speed range.

5) Steady-state torque-sharing

The multi-three-phase machines are often employed in applications where power levels approach the megawatt. In these contexts, the full-load-tests of the machine become very hard to be performed since the prime mover is often not available. For this reason, regenerative tests can be performed, using back-to-back configurations [42]. Such configurations consist of operating some units in motoring and others in the generation, keeping the machine torque at zero.

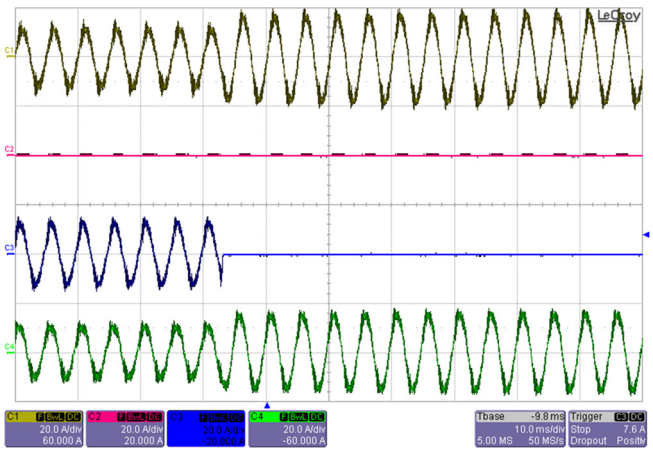

Fig. 24. Phase-currents obtained by performing test 3) with the conventional MS-based DFVC scheme [7]. Ch1: $i_{s1\text{-}a}$ (20 A/div), Ch2: $i_{s2\text{-}a}$ (20 A/div), Ch3: $i_{s3\text{-}a}$ (20 A/div), Ch4: $i_{s4\text{-}a}$ (20 A/div). Time resolution: 10 ms/div.

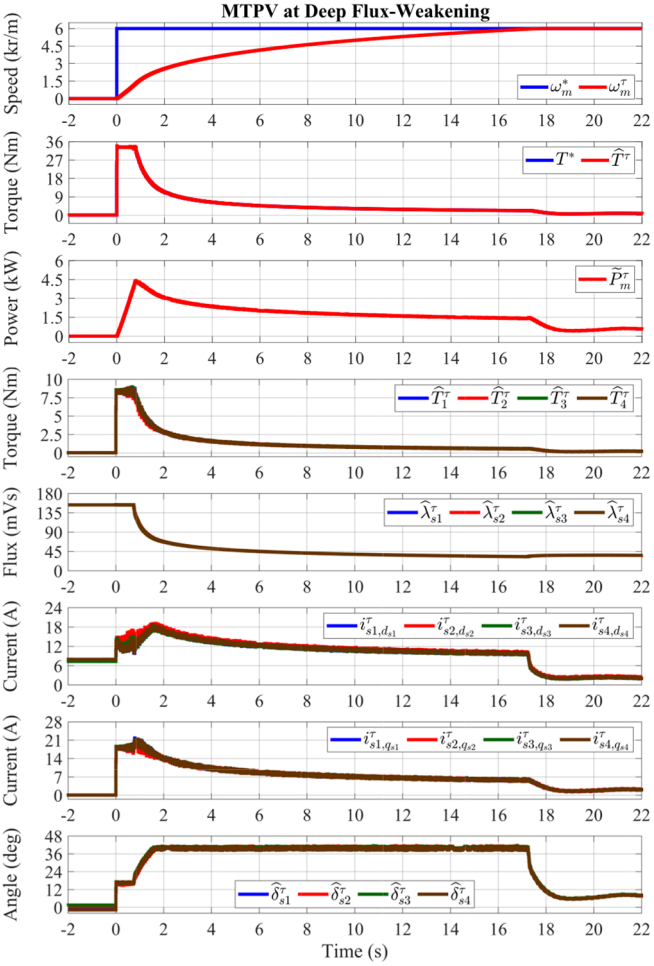

Fig. 25. Closed-loop speed control with inertial load from 0 to 6000 r/m.

In this way, if the units operate at their maximum power, only machine- and converter- losses are produced. In this work, the back-to-back configuration has been tested by performing torque-sharing strategies among the sets, as shown in Figs. 26 - 27.

The same conditions of test 1) in terms of dc-link voltage and machine speed have been employed. The torque reference of the units 1 and 4 has been set at 6 Nm (150% rated torque in generation). Conversely, the torque reference of the units 2 and 3 has been set at – 6 Nm (150% rated torque in motoring). It is noted how, although the electromagnetic power of each set is about 3.8 kW (absolute value), the machine torque/power is kept at zero.

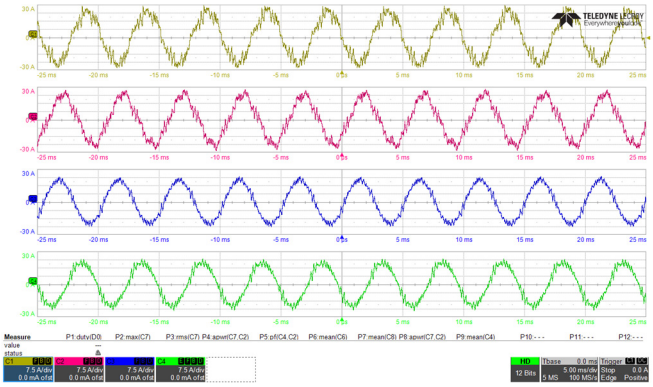

Fig. 26. Back-to-back configuration with overload 150 % at -6000 r/m. Ch1: $i_{s1\text{-}a}$ (7.5 A/div), Ch2: $i_{s2\text{-}a}$ (7.5 A/div), Ch3: $i_{s3\text{-}a}$ (7.5 A/div), Ch4: $i_{s4\text{-}a}$ (7.5 A/div). Time resolution: 5 ms/div.

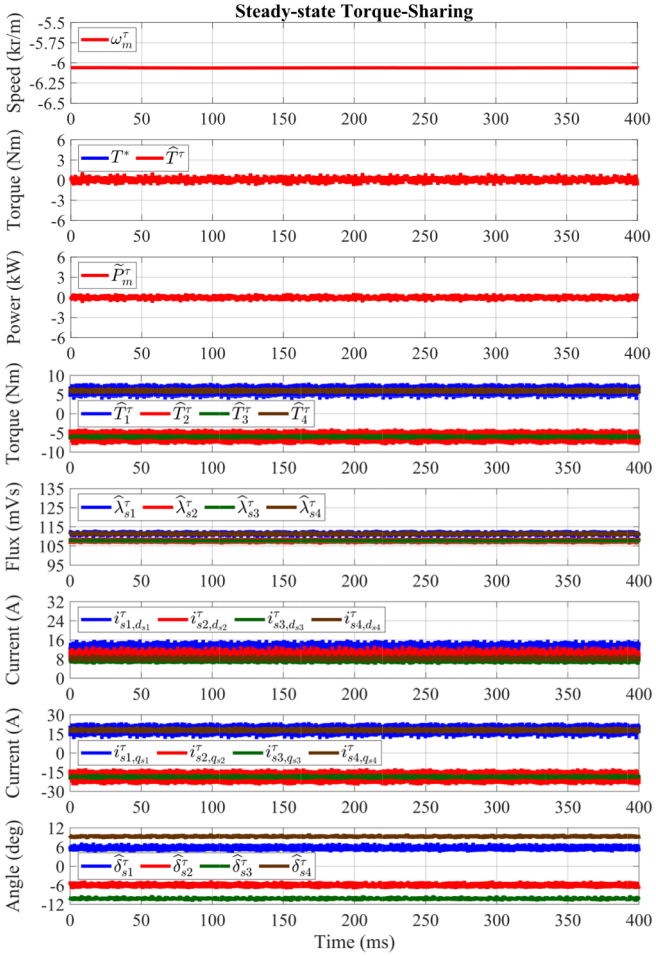

Fig. 27. Back-to-back configuration with overload 150 % at -6000 r/m.

Compared to the previous tests, it is noted a derating of the quality of the waveforms, as confirmed in Figs. 26-27. Indeed, the back-to-back configurations lead to relevant distortion effects on the magnetomotive force at the machine airgap. However, through this test, the torque-sharing operation among the sets in steady-state conditions has been validated.

6) Sinusoidal torque-sharing

The full validation of the decoupling algorithm has been carried out through sinusoidal torque-sharing tests performed in deep flux-weakening. The dc-link voltage has been reduced at 100 V, while the mechanical speed has been initially set at -4000 r/m to avoid the MTPV.

For each unit, a base reference torque of 1.5 Nm has been set. Besides, an oscillation having an amplitude of 3 Nm, and a frequency of 10 Hz has been added.

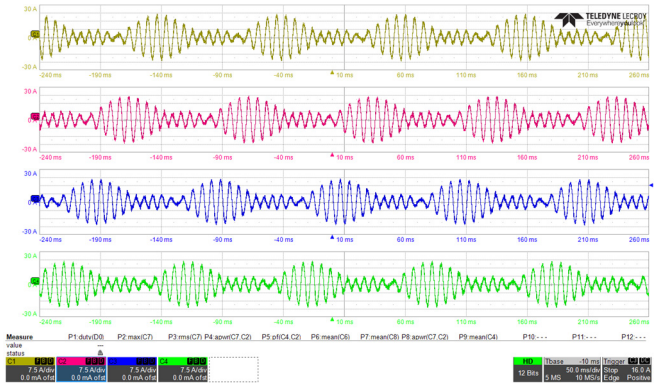

Fig. 28. Sinusoidal torque-sharing in flux-weakening at -4000 r/m, 6 Nm. Ch1: $i_{s1\text{-}a}$ (7.5 A/div), Ch2: $i_{s2\text{-}a}$ (7.5 A/div), Ch3: $i_{s3\text{-}a}$ (7.5 A/div), Ch4: $i_{s4\text{-}a}$ (7.5 A/div). Time resolution: 50 ms/div.

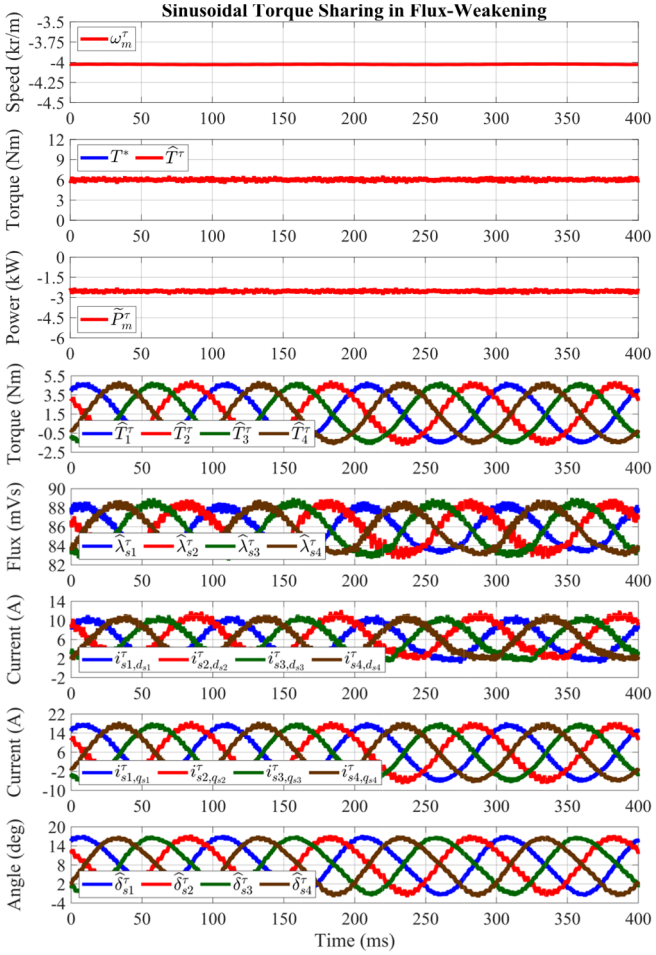

Fig. 29. Sinusoidal torque-sharing in flux-weakening at -4000 r/m, 6 Nm.

The torque oscillations among the sets have been shifted each other in time, emulating a symmetrical four-phase system. In this way, while the sets' torques have always been kept different from each other, their sum was constant (6 Nm). The obtained experimental results are shown in Figs. 28 - 29.

It is noted how, at any moment, some units have been operated in generation mode, while the others have been operated in motoring mode. Although this test does not have a direct application, it has demonstrated the torque-sharing capability of the proposed solution in dynamic conditions. Indeed, the variables of each set in terms of flux amplitude, currents, and load-angle change sinusoidally. In detail, the flux amplitude oscillation of each set is generated by the DFVC scheme controlling it, allowing the respect of the voltage limit at any moment.

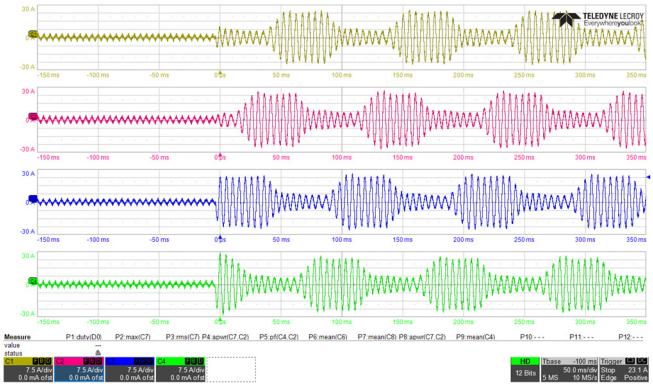

Fig. 30. Sinusoidal torque-sharing with modular MTPV at -6000 r/m, 5 Nm. Ch1: $i_{s1\text{-}a}$ (7.5 A/div), Ch2: $i_{s2\text{-}a}$ (7.5 A/div), Ch3: $i_{s3\text{-}a}$ (7.5 A/div), Ch4: $i_{s4\text{-}a}$ (7.5 A/div). Time resolution: 50 ms/div.

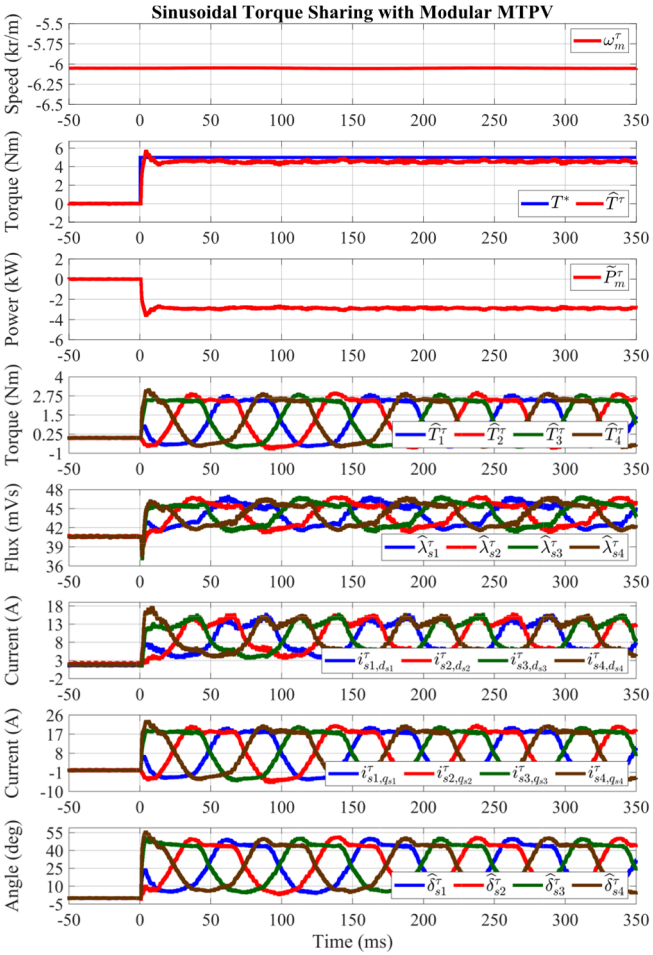

Fig. 31. Sinusoidal torque-sharing with modular MTPV at -6000 r/m, 5 Nm.

Concerning Fig. 28, the oscillations of the phase-currents are similar to those of the radio waves using amplitude modulation. However, for each set, this oscillation (10 Hz) corresponds to a power of 1.2 kW (average value of -600 W).

The torque-sharing capability has also been tested in MTPV operation. The machine speed has been set at -6000 r/m, while the overall torque reference has been initially kept at zero, performing the no-load operation. From a specific time instant onwards, the torque reference of the machine has been suddenly set to 5 Nm (-3.1 kW). Therefore, for each unit, a base reference torque of 1.25 Nm has been set. However, the sinusoidal torque-sharing operation has been enabled too. The torque oscillation of each unit has been set at 2.5 Nm (1.6 kW) with a frequency of 10 Hz. The experimental results are shown in Figs. 30 - 31.

It is noted how the torque reference of each set has not been fulfilled continuously. Indeed, the DFVC scheme of each unit has performed a proper saturation of its torque-producing current reference, thus limiting the load-angle to the MTPV value ($\delta_{max,k}$ = 45 electrical degrees, k=1,2,3,4).

It is highlighted the wide oscillation range of each set's load-angle, from about 0 up to 45 electrical degrees. Besides, a significant angular difference among the stator frames of the units is obtained, up to 45 degrees (Fig. 31). Therefore, through this last test, the effectiveness of the proposed decoupling algorithm has been fully demonstrated.

V. Conclusion

The paper proposes a control scheme for the modular regulation of the stator flux and torque of a multi-three-phase induction machine (IM). Through the direct control of the torque contribution of each set, the proposed solution allows the implementation of power-sharing strategies. Besides, the application of an innovative decoupling algorithm solves any instability issue introduced by the modular approach (multi-stator). The proposed control scheme can deal with the voltage and current constraints of voltage source inverters feeding the sets, allowing the deep flux-weakening operation. Also, the direct limitation of each set's load-angle allows the implementation of modular maximum-torque per voltage (MTPV) strategies, avoiding the machine pull-out.

The performance of the proposed control solution has been validated on a twelve-phase squirrel-cage IM prototype, using a quadruple-three-phase configuration of the stator winding. The experimental results demonstrate the feasibility of the proposed control scheme both in regular and faulty operation (open-winding faults), as well as the torque-sharing capability in deep flux-weakening operation with MTPV. Therefore, the adding value of this paper to the existing literature can be summarized as follows:

- A new decoupling algorithm has been introduced, allowing control stability and high regulation performance if power-sharing strategies among the sets are performed.
- A control solution performing a direct and independent limitation of the load-angle of each set has been implemented, allowing modular MTPV strategies at flux-weakening.
- The power-sharing strategies among the units are performed through the modular torque control, where the torque produced by each set is linearly controlled.

Appendix

1) Computation of the k-set torque contribution T_k

The torque contribution of each three-phase winding set is computed by performing the power balance of the machine. The IM model (2), (4)-(6) in stationary coordinates (αβ) is considered, leading to as follows:

$$\bar{v}_{sk,\alpha\beta} = R_{sk} \cdot \bar{i}_{sk,\alpha\beta} + \frac{d}{dt}\bar{\lambda}_{sk,\alpha\beta} \tag{32}$$

$$\begin{bmatrix} 0 & 0 \end{bmatrix}^t = R_r \cdot \bar{i}_{r,\alpha\beta} + \frac{d}{dt}\bar{\lambda}_{r,\alpha\beta} - j \cdot \omega_e \cdot \bar{\lambda}_{r,\alpha\beta} \tag{33}$$

$$\bar{\lambda}_{r,\alpha\beta} = L_{lr} \cdot \bar{i}_{r,\alpha\beta} + L_m \cdot \sum_{z=1}^{n} \bar{i}_{sz,\alpha\beta} + L_m \cdot \bar{i}_{r,\alpha\beta} \tag{34}$$

$$\bar{\lambda}_{sk,\alpha\beta} = k_r \cdot \bar{\lambda}_{r,\alpha\beta} + L_{lsk} \cdot \bar{i}_{sk,\alpha\beta} + k_r \cdot L_{lr} \cdot \sum_{z=1}^{n} \bar{i}_{sz,\alpha\beta} \tag{35}$$

Based on (32), (33), the electric power P_e of the machine (instantaneous) is computed as:

$$P_e = \frac{3}{2}\cdot\sum_{k=1}^{n}\left(\bar{i}_{sk,\alpha\beta}^{t}\cdot\bar{v}_{sk,\alpha\beta}\right)+\frac{3}{2}\cdot\bar{i}_{r,\alpha\beta}^{t}\cdot\begin{bmatrix}0 & 0\end{bmatrix}^{t} = P_J + P_{mag} + P_m \tag{36}$$

where the coefficient 3/2 derives from the amplitude-invariant propriety of the Clarke transformation (1), while the Joule losses P_J, the magnetizing power P_{mag}, and mechanical power P_m are computed as:

$$\begin{aligned} P_J &= \frac{3}{2}\cdot\sum_{k=1}^{n}\left(R_{sk}\cdot\bar{i}_{sk,\alpha\beta}^{t}\cdot\bar{i}_{sk,\alpha\beta}\right)+\frac{3}{2}\cdot R_r\cdot\bar{i}_{r,\alpha\beta}^{t}\cdot\bar{i}_{r,\alpha\beta} \\ P_{mag} &= \frac{3}{2}\cdot\sum_{k=1}^{n}\left(\bar{i}_{sk,\alpha\beta}^{t}\cdot\frac{d}{dt}\bar{\lambda}_{sk,\alpha\beta}\right)+\frac{3}{2}\cdot\bar{i}_{r,\alpha\beta}^{t}\cdot\frac{d}{dt}\bar{\lambda}_{r,\alpha\beta} \\ P_m &= -\frac{3}{2}\cdot\omega_e\cdot\bar{i}_{r,\alpha\beta}^{t}\cdot j\cdot\bar{\lambda}_{r,\alpha\beta} = \frac{3}{2}\cdot p\cdot\omega_m\cdot\left(\bar{i}_{r,\alpha\beta}\wedge\bar{\lambda}_{r,\alpha\beta}\right) \end{aligned} \tag{37}$$

From the mechanical power P_m (37), the machine torque T is obtained as:

$$T = \frac{P_m}{\omega_m} = \frac{3}{2}\cdot p\cdot\left(\bar{i}_{r,\alpha\beta}\wedge\bar{\lambda}_{r,\alpha\beta}\right) \tag{38}$$

where, as for a 3-phase IM, it is noted how it depends on the cross-product ($\wedge$) between the rotor vectors of current and flux linkage. By replacing (34) in (38), the torque expression becomes:

$$T = \frac{3}{2}\cdot p\cdot\left(k_r\cdot\bar{\lambda}_{r,\alpha\beta}\wedge\sum_{k=1}^{n}\bar{i}_{sk,\alpha\beta}\right) = \frac{3}{2}\cdot p\cdot\sum_{k=1}^{n}\left(k_r\cdot\bar{\lambda}_{r,\alpha\beta}\wedge\bar{i}_{sk,\alpha\beta}\right) \tag{39}$$

where the summation index has been formally changed from z to k. However, according to (35), the first term of the outer product can be written as:

$$k_r\cdot\bar{\lambda}_{r,\alpha\beta} = \bar{\lambda}_{sk,\alpha\beta} - L_{lsk}\cdot\bar{i}_{sk,\alpha\beta} - k_r\cdot L_{lr}\cdot\sum_{z=1}^{n}\bar{i}_{sz,\alpha\beta} \tag{40}$$

Therefore, by replacing (40) in (39), the machine torque is computed as follows:

$$T = \frac{3}{2}\cdot p\cdot\sum_{k=1}^{n}\left(\bar{\lambda}_{sk,\alpha\beta}\wedge\bar{i}_{sk,\alpha\beta}\right) = \sum_{k=1}^{n}T_k \tag{41}$$

where the expression of the k-set torque contribution T_k (k = 1,2,..,n) is extracted directly as:

$$T_k = \frac{3}{2}\cdot p\cdot\left(\bar{\lambda}_{sk,\alpha\beta}\wedge\bar{i}_{sk,\alpha\beta}\right) \tag{42}$$

Finally, since the cross-product does not depend on the frame in which the vectors are referred, the k-set torque contribution (42) can be also expressed as in (43), thus proving (7).

$$T_k = \frac{3}{2}\cdot p\cdot\left(\bar{\lambda}_{sk,xy}\wedge\bar{i}_{sk,xy}\right) \tag{43}$$

2) Decoupling equation

The coefficients of the decoupling equation (31) are computed as follows:

$$s_{(k,k)}^{\tau+1} = \frac{1}{S_c^{\tau+1}}\cdot\left[\left(1+\tilde{w}_k^{\tau}\right)+\frac{1}{2}\cdot\left(1+\sum_{l=1}^{n}\tilde{w}_l^{\tau}\right)^{-1}\cdot S_{k-k}^{\tau+1}\right] \tag{44}$$

$$s_{(k,z)}^{\tau+1} = \frac{1}{S_c^{\tau+1}}\cdot\left[\tilde{w}_z^{\tau}\cdot\left(1+\sum_{l=1}^{n}\tilde{w}_l^{\tau}\right)^{-1}\cdot S_{k-z}^{\tau+1}\right] \tag{45}$$

where:

$$S_c^{\tau+1} = \left(1+\sum_{l=1}^{n}\tilde{w}_l^{\tau}\right)+\frac{1}{2}\cdot\sum_{l=1}^{n}\sum_{g=1}^{n}\left[\tilde{w}_l^{\tau}\cdot\tilde{w}_g^{\tau}\cdot\sin^2\left(\hat{\delta}_{sl}^{\tau+1}-\hat{\delta}_{sg}^{\tau+1}\right)\right] \tag{46}$$

$$S_{k-k}^{\tau+1} = \sum_{\substack{l=1\\l\neq k}}^{n}\sum_{\substack{g=1\\g\neq k}}^{n}\left[\tilde{w}_l^{\tau}\cdot\tilde{w}_g^{\tau}\cdot\sin^2\left(\hat{\delta}_{sl}^{\tau+1}-\hat{\delta}_{sg}^{\tau+1}\right)\right] \tag{47}$$

$$\begin{aligned} S_{k-z}^{\tau+1} &= \left(1+\tilde{w}_k^{\tau}+\tilde{w}_z^{\tau}\right)\cdot\cos\left(\hat{\delta}_{sk}^{\tau+1}-\hat{\delta}_{sz}^{\tau+1}\right)+... \\ &...+\sum_{l=1,l\neq k,z}^{n}\left[\tilde{w}_l^{\tau}\cdot\cos\left(\hat{\delta}_{sk}^{\tau+1}-\hat{\delta}_{sl}^{\tau+1}\right)\cdot\cos\left(\hat{\delta}_{sz}^{\tau+1}-\hat{\delta}_{sl}^{\tau+1}\right)\right] \end{aligned} \tag{48}$$

It is highlighted how the computation of the decoupling coefficients (46)-(48) does not require the evaluation of the load-angles of the sets for the next sample time instant τ+1. Indeed, if considering two generic sets k and z, the difference of the related load-angles in terms of sine and cosine can be computed as:

$$\begin{aligned} &\cos\left(\hat{\delta}_{sk}^{\tau+1}-\hat{\delta}_{sz}^{\tau+1}\right) = \cos\left(\hat{\vartheta}_{\lambda-sk}^{\tau+1}-\hat{\vartheta}_{\lambda-sz}^{\tau+1}\right) = ... \\ &...=\cos\left(\hat{\vartheta}_{\lambda-sk}^{\tau+1}\right)\cdot\cos\left(\hat{\vartheta}_{\lambda-sz}^{\tau+1}\right)+\sin\left(\hat{\vartheta}_{\lambda-sk}^{\tau+1}\right)\cdot\sin\left(\hat{\vartheta}_{\lambda-sz}^{\tau+1}\right) \\ &\sin\left(\hat{\delta}_{sk}^{\tau+1}-\hat{\delta}_{sz}^{\tau+1}\right) = \sin\left(\hat{\vartheta}_{\lambda-sk}^{\tau+1}-\hat{\vartheta}_{\lambda-sz}^{\tau+1}\right) = ... \\ &...=\sin\left(\hat{\vartheta}_{\lambda-sk}^{\tau+1}\right)\cdot\cos\left(\hat{\vartheta}_{\lambda-sz}^{\tau+1}\right)-\cos\left(\hat{\vartheta}_{\lambda-sk}^{\tau+1}\right)\cdot\sin\left(\hat{\vartheta}_{\lambda-sz}^{\tau+1}\right) \end{aligned} \tag{49}$$

where it is shown how the decoupling coefficients can be computed using the trigonometric coordinates of the positions of the stator flux vectors for the next sample time instant τ+1, and thus obtained from the flux observers of the units directly (Fig. 7). In the following, the computation of the decoupling equation (31) for some practical cases is shown, facilitating the understanding.

a) Balanced operation of units

Multi-three-phase machines are often operated without performing torque-sharing operations among the units. In this case, the load-angles of the sets are equal to each other, leading to the following decoupling equation:

$$v_{sk,q_{sk}}^{*} = \left(1+\sum_{l=1}^{n}\tilde{w}_l^{\tau}\right)^{-1}\cdot\left[F_{sk,q_{sk}}^{*}+\sum_{z=1}^{n}\left(\tilde{w}_z^{\tau}\cdot F_{sz,q_{sz}}^{*}\right)\right] \tag{50}$$

that correspond to the solution implemented in [26]. Indeed, the decoupling coefficients (44)-(48) and the variables in (30) are simplified as:

$$\begin{cases} S_c^{\tau+1} = S_{k-z}^{\tau+1} = \left(1+\sum_{l=1}^{n}\tilde{w}_l^{\tau}\right) \\ S_{k-k}^{\tau+1} = 0 \end{cases} \Rightarrow \begin{cases} s_{(k-k)}^{\tau+1} = \dfrac{\left(1+\tilde{w}_k^{\tau}\right)}{\left(1+\sum_{l=1}^{n}\tilde{w}_l^{\tau}\right)} \\ s_{(k-z)}^{\tau+1} = \dfrac{\tilde{w}_z^{\tau}}{\left(1+\sum_{l=1}^{n}\tilde{w}_l^{\tau}\right)} \end{cases} \tag{51}$$

$$C_{sk,q_{sk}}^{*} = F_{sk,q_{sk}}^{*} \tag{52}$$

b) Dual-three-phase configuration

Based on the literature [1]–[3], the most employed multi-three-phase configuration in the industry is the dual-three-phase (n = 2). By denoting with δ the difference between the load-angle of set 1 to that of set 2 (δ_{s2} - δ_{s1}), the q_{sk}-axis reference voltage of each unit k (k=1,2) is computed as:

$$
\begin{aligned}
v^*_{s1,q_{s1}} &= s^{\tau+1}_{(1,1)} \cdot C^*_{s1,q_{s1}} + s^{\tau+1}_{(1,2)} \cdot C^*_{s2,q_{s2}} \\
v^*_{s2,q_{s2}} &= s^{\tau+1}_{(2,2)} \cdot C^*_{s2,q_{s2}} + s^{\tau+1}_{(2,1)} \cdot C^*_{s1,q_{s1}}
\end{aligned} \tag{53}
$$

where:

$$
\begin{aligned}
C^*_{s1,q_{s1}} &= F^*_{s1,q_{s1}} - \tilde{w}^{\tau}_2 \cdot v^*_{s2,d_{s2}} \cdot \sin\left(\hat{\delta}^{\tau+1}\right) \\
C^*_{s2,q_{s2}} &= F^*_{s2,q_{s2}} + \tilde{w}^{\tau}_1 \cdot v^*_{s1,d_{s1}} \cdot \sin\left(\hat{\delta}^{\tau+1}\right)
\end{aligned} \tag{54}
$$

The decoupling coefficients (44), (45) are computed as:

$$
\begin{aligned}
s^{\tau+1}_{(1,1)} &= \frac{1+w^{\tau}_1}{1+w^{\tau}_1+w^{\tau}_2+w^{\tau}_1 \cdot w^{\tau}_2 \cdot \sin^2\left(\hat{\delta}^{\tau+1}\right)} \\
s^{\tau+1}_{(1,2)} &= \frac{w^{\tau}_2 \cdot \cos\left(\hat{\delta}^{\tau+1}\right)}{1+w^{\tau}_1+w^{\tau}_2+w^{\tau}_1 \cdot w^{\tau}_2 \cdot \sin^2\left(\hat{\delta}^{\tau+1}\right)} \\
s^{\tau+1}_{(1,1)} &= \frac{1+w^{\tau}_2}{1+w^{\tau}_1+w^{\tau}_2+w^{\tau}_1 \cdot w^{\tau}_2 \cdot \sin^2\left(\hat{\delta}^{\tau+1}\right)} \\
s^{\tau+1}_{(2,1)} &= \frac{w^{\tau}_1 \cdot \cos\left(\hat{\delta}^{\tau+1}\right)}{1+w^{\tau}_1+w^{\tau}_2+w^{\tau}_1 \cdot w^{\tau}_2 \cdot \sin^2\left(\hat{\delta}^{\tau+1}\right)}
\end{aligned} \tag{55}
$$

since (46)-(48) becomes:

$$
\begin{aligned}
S^{\tau+1}_c &= 1+w^{\tau}_1+w^{\tau}_2+w^{\tau}_1 \cdot w^{\tau}_2 \cdot \sin^2\left(\hat{\delta}^{\tau+1}\right) \\
S^{\tau+1}_{1-1} &= S^{\tau+1}_{2-2} = 0 \\
S^{\tau+1}_{1-2} &= S^{\tau+1}_{2-1} = \left(1+w^{\tau}_1+w^{\tau}_2\right) \cdot \cos\left(\hat{\delta}^{\tau+1}\right)
\end{aligned} \tag{56}
$$

REFERENCES

[1] E. Levi, 'Multiphase Electric Machines for Variable-Speed Applications', *IEEE Trans. Ind. Electron.*, vol. 55, no. 5, pp. 1893–1909, May 2008.

[2] R. Bojoi, S. Rubino, A. Tenconi, and S. Vaschetto, 'Multiphase electrical machines and drives: A viable solution for energy generation and transportation electrification', in *2016 International Conference and Exposition on Electrical and Power Engineering (EPE)*, Oct. 2016, pp. 632–639.

[3] F. Barrero and M. J. Duran, 'Recent Advances in the Design, Modeling, and Control of Multiphase Machines—Part I', *IEEE Trans. Ind. Electron.*, vol. 63, no. 1, pp. 449–458, Jan. 2016.

[4] M. J. Duran and F. Barrero, 'Recent Advances in the Design, Modeling, and Control of Multiphase Machines—Part II', *IEEE Trans. Ind. Electron.*, vol. 63, no. 1, pp. 459–468, Jan. 2016.

[5] W. Cao, B. C. Mecrow, G. J. Atkinson, J. W. Bennett, and D. J. Atkinson, 'Overview of Electric Motor Technologies Used for More Electric Aircraft (MEA)', *IEEE Trans. Ind. Electron.*, vol. 59, no. 9, pp. 3523–3531, Sep. 2012.

[6] A. Tessarolo, G. Zocco, and C. Tonello, 'Design and Testing of a 45-MW 100-Hz Quadruple-Star Synchronous Motor for a Liquefied Natural Gas Turbo-Compressor Drive', *IEEE Trans. Ind. Appl.*, vol. 47, no. 3, pp. 1210–1219, May 2011.

[7] S. Rubino, R. Bojoi, A. Cavagnino, and S. Vaschetto, 'Asymmetrical twelve-phase induction starter/generator for more electric engine in aircraft', in *2016 IEEE Energy Conversion Congress and Exposition (ECCE)*, Sep. 2016, pp. 1–8.

[8] R. Bojoi, A. Cavagnino, A. Tenconi, and S. Vaschetto, 'Control of Shaft-Line-Embedded Multiphase Starter/Generator for Aero-Engine', *IEEE Trans. Ind. Electron.*, vol. 63, no. 1, pp. 641–652, Jan. 2016.

[9] E. Jung, H. Yoo, S. Sul, H. Choi, and Y. Choi, 'A Nine-Phase Permanent-Magnet Motor Drive System for an Ultrahigh-Speed Elevator', *IEEE Trans. Ind. Appl.*, vol. 48, no. 3, pp. 987–995, May 2012.

[10] K. Hatua and V. T. Ranganathan, 'Direct torque control schemes for split-phase induction machine', *IEEE Trans. Ind. Appl.*, vol. 41, no. 5, pp. 1243–1254, Sep. 2005.

[11] S. Rubino, R. Bojoi, E. Levi, and O. Dordevic, 'Vector Control of Multiple Three-Phase Permanent Magnet Motor Drives', in *IECON 2018 - 44th Annual Conference of the IEEE Industrial Electronics Society*, Oct. 2018, pp. 5866–5871.

[12] I. Zoric, M. Jones, and E. Levi, 'Arbitrary d–q current sharing in three-phase winding sets of multi-phase machines', *J. Eng.*, vol. 2019, no. 17, pp. 4173–4177, 2019.

[13] A. Galassini, A. Costabeber, M. Degano, C. Gerada, A. Tessarolo, and R. Menis, 'Enhanced Power Sharing Transient With Droop Controllers for Multithree-Phase Synchronous Electrical Machines', *IEEE Trans. Ind. Electron.*, vol. 66, no. 7, pp. 5600–5610, Jul. 2019.

[14] G. Sala, M. Mengoni, G. Rizzoli, L. Zarri, and A. Tani, 'Decoupled d-q Axes Current Sharing Control of Multi Three-Phase Induction Machines', *IEEE Trans. Ind. Electron.*, vol. 67, no. 9, pp. 7124–7134, Sep. 2020.

[15] I. Zoric, M. Jones, and E. Levi, 'Arbitrary Power Sharing Among Three-Phase Winding Sets of Multiphase Machines', *IEEE Trans. Ind. Electron.*, vol. 65, no. 2, pp. 1128–1139, Feb. 2018.

[16] M. J. Durán, S. Kouro, B. Wu, E. Levi, F. Barrero, and S. Alepuz, 'Six-phase PMSG wind energy conversion system based on medium-voltage multilevel converter', in *Proceedings of the 2011 14th European Conference on Power Electronics and Applications*, Aug. 2011, pp. 1–10.

[17] I. Zoric, M. Jones, and E. Levi, 'Voltage balancing control of a symmetrical nine-phase machine with series-connected DC links', in *2017 IEEE 26th International Symposium on Industrial Electronics (ISIE)*, Jun. 2017, pp. 1052–1057.

[18] F. Blaabjerg and Z. Chen, *Power Electronics for Modern Wind Turbines*. Morgan & Claypool, 2006.

[19] Y. Zhao and T. A. Lipo, 'Space vector PWM control of dual three-phase induction machine using vector space decomposition', *IEEE Trans. Ind. Appl.*, vol. 31, no. 5, pp. 1100–1109, Sep. 1995.

[20] I. Zoric, M. Jones, and E. Levi, 'Vector space decomposition algorithm for asymmetrical multiphase machines', in *2017 International Symposium on Power Electronics (Ee)*, Oct. 2017, pp. 1–6.

[21] Y. Hu, Z. Q. Zhu, and M. Odavic, 'Comparison of Two-Individual Current Control and Vector Space Decomposition Control for Dual Three-Phase PMSM', *IEEE Trans. Ind. Appl.*, vol. 53, no. 5, pp. 4483–4492, Sep. 2017.

[22] R. Bojoi, F. Farina, G. Griva, F. Profumo, and A. Tenconi, 'Direct torque control for dual three-phase induction motor drives', *IEEE Trans. Ind. Appl.*, vol. 41, no. 6, pp. 1627–1636, Nov. 2005.

[23] J. K. Pandit, M. V. Aware, R. V. Nemade, and E. Levi, 'Direct Torque Control Scheme for a Six-Phase Induction Motor With Reduced Torque Ripple', *IEEE Trans. Power Electron.*, vol. 32, no. 9, pp. 7118–7129, Sep. 2017.

[24] R. H. Nelson and P. C. Krause, 'Induction Machine Analysis for Arbitrary Displacement Between Multiple Winding Sets', *IEEE Trans. Power Appar. Syst.*, vol. PAS-93, no. 3, pp. 841–848, May 1974.

[25] R. Bojoi, M. Lazzari, F. Profumo, and A. Tenconi, 'Digital field-oriented control for dual three-phase induction motor drives', *IEEE Trans. Ind. Appl.*, vol. 39, no. 3, pp. 752–760, May 2003.

[26] S. Rubino, R. Bojoi, S. A. Odhano, and P. Zanchetta, 'Model Predictive Direct Flux Vector Control of Multi-three-Phase Induction Motor Drives', *IEEE Trans. Ind. Appl.*, vol. 54, no. 5, pp. 4394–4404, Sep. 2018.

[27] S. Rubino, R. Bojoi, D. Cittanti, and L. Zarri, 'Decoupled and Modular Torque Control of Multi-Three-Phase Induction Motor Drives', *IEEE Trans. Ind. Appl.*, 2020.

[28] Bon-Ho Bae, N. Patel, S. Schulz, and Seung-Ki Sul, 'New field weakening technique for high saliency interior permanent magnet motor', in *38th IAS Annual Meeting on Conference Record of the Industry Applications Conference, 2003.*, Oct. 2003, vol. 2, pp. 898–905 vol.2.

[29] G. Pellegrino, R. I. Bojoi, and P. Guglielmi, 'Unified Direct-Flux Vector Control for AC Motor Drives', *IEEE Trans. Ind. Appl.*, vol. 47, no. 5, pp. 2093–2102, Sep. 2011.

[30] S. Rubino, R. Bojoi, F. Mandrile, and E. Armando, 'Modular Stator Flux and Torque Control of Multiphase Induction Motor Drives', in *2019 IEEE International Electric Machines and Drives Conference (IEMDC)*, San Diego, USA, 2019, pp. 531–538.

[31] P. Krause, O. Wasynczuk, S. D. Sudhoff, and S. Pekarek, *Analysis of Electric Machinery and Drive Systems*. John Wiley & Sons, 2013.

[32] A. Boglietti, R. Bojoi, S. Rubino, and M. Cossale, 'Overload Capability of Multiphase Machines under Normal and Open-Phase Fault Conditions: a Thermal Analysis Approach', *IEEE Trans. Ind. Appl.*, vol. 56, no. 3, pp. 2560–2569, Mar. 2020.

[33] A. S. Abdel-Khalik, A. M. Massoud, and S. Ahmed, 'Application of Standard Three-Phase Stator Frames in Prime Phase Order Multiphase Machine Construction', *IEEE Trans. Ind. Electron.*, vol. 66, no. 4, pp. 2506–2517, Apr. 2019.

[34] S. Rubino, R. Bojoi, M. Mengoni, and L. Zarri, 'Optimal flux selection for multi three-phase machines in normal and fault conditions', in *2017 IEEE International Electric Machines and Drives Conference (IEMDC)*, May 2017, pp. 1–8.

[35] P. L. Jansen and R. D. Lorenz, 'A physically insightful approach to the design and accuracy assessment of flux observers for field oriented induction machine drives', *IEEE Trans. Ind. Appl.*, vol. 30, no. 1, pp. 101–110, Jan. 1994.

[36] G. Pellegrino, R. I. Bojoi, P. Guglielmi, and F. Cupertino, 'Accurate Inverter Error Compensation and Related Self-Commissioning Scheme in Sensorless Induction Motor Drives', *IEEE Trans. Ind. Appl.*, vol. 46, no. 5, pp. 1970–1978, Sep. 2010.

[37] D. G. Holmes and T. A. Lipo, *Pulse Width Modulation for Power Converters: Principles and Practice*. John Wiley & Sons, 2003.

[38] A. M. Hava, R. J. Kerkman, and T. A. Lipo, 'A high-performance generalized discontinuous PWM algorithm', *IEEE Trans. Ind. Appl.*, vol. 34, no. 5, pp. 1059–1071, Sep. 1998.

[39] G. Rizzoli, G. Serra, P. Maggiore, and A. Tenconi, 'Optimized design of a multiphase induction machine for an open rotor aero-engine shaft-line-embedded starter/generator', in *IECON 2013 - 39th Annual Conference of the IEEE Industrial Electronics Society*, Nov. 2013, pp. 5203–5208.

[40] F. Mariut, S. Rosu, R. Bojoi, and A. Tenconi, 'Multiphase modular power converter using the PEBB concept and FPGA-based direct high speed voltage measurement', in *2015 17th European Conference on Power Electronics and Applications (EPE'15 ECCE-Europe)*, Sep. 2015, pp. 1–10.

[41] Sang-Hoon Kim and Seung-Ki Sul, 'Maximum torque control of an induction machine in the field weakening region', *IEEE Trans. Ind. Appl.*, vol. 31, no. 4, pp. 787–794, Jul. 1995.

[42] A. A. Abduallah, O. Dordevic, M. Jones, and E. Levi, 'Regenerative Test for Multiple Three-Phase Machines With Even Number of Neutral Points', *IEEE Trans. Ind. Electron.*, vol. 67, no. 3, pp. 1684–1694, Mar. 2020.